THE INVESTIGATION OF THE PREPARATION OF $Al_xGa_{1-x}As$ DOUBLE HETEROSTRUCTURE LASER DIODES BY LIQUID PHASE EPITAXY

by

Terence G. Blake

PART A: INDUSTRIAL PROJECT*

A project report submitted in partial fulfillment of the
requirements for the degree of
Master of Engineering

The work reported upon herein was undertaken at the
Bell-Northern Research, Ottawa, Ontario

Dept. of Engineering Physics
McMaster University
Hamilton, Ontario

1972

* One of two project reports. The other part is designated PART B: McMASTER (ON-CAMPUS) PROJECT.

Title (Part A): The Investigation of the Preparation of $Al_xGa_{1-x}As$ Double Heterostructure Laser Diodes by Liquid Phase Epitaxy

AUTHOR: Terence G. Blake, B.Sc. (Physics) - University of Calgary

SUPERVISOR: Dr. A. J. SpringThorpe

NUMBER OF PAGES: 41

MASTER OF ENGINEERING
(Engineering Physics)

McMASTER UNIVERSITY
Hamilton, Ontario

ACKNOWLEDGEMENTS

I am extremely grateful to the following for their contributions to this work.

Dr. A.J. SpringThorpe, for a great deal of instruction and encouragement; R. Abbott, A. Becke, and C. Quinn for their assistance in the lab; H. Becke, for constructing the quartzware; R. Abbott again, and E.M. Russell and I. Thomson, for fabricating and testing the laser chips; W.M. Coderre and P. Garel-Jones for doing the photoluminescence and spectroanalysis; Drs. R.R. Ferguson, J. Taylor, and G. Rosenthal for helpful discussions; Mrs. E.A. Stenson for the typing; and Bell-Northern Research, which provided the facilities and materials that made the work possible.

INTRODUCTION

The electroluminescent properties of gallium arsenide are well known and led to the first observation, in 1962, of stimulated coherent emission from a semiconductor, a GaAs junction diode (1). Since then, room temperature CW-mode junction lasers have been reported (2).

Stimulated emission in a pn-junction laser occurs when a high injection of carriers across the junction produces population inversion in the "active" region, which normally extends on the order of a diffusion length away from the junction. It was suggested by Kroemer (3) that if the active region were bounded by a material having a band gap slightly larger than that of GaAs, then a potential barrier would confine the carriers, and a refractive index barrier would confine the light. If the active region is thereby reduced to less than a diffusion length, the carrier injection and the carrier-photon coupling will be significantly improved and the lasing threshold lowered (4,5,6,).

The confinement material chosen was aluminum gallium arsenide, because the aluminum arsenide lattice spacings are no more than 0.2% different from those of gallium arsenide. This means that the barrier interface will have negligibly few mid-gap, non-radiative recombination centres. Since AlAs has a band gap at $300^{\circ}K$ of 2.2 eV (7) while that of GaAs is 1.43 eV (8), the alloy has the desired confinement properties.

The effect is more pronounced when the n-side of the junction is also composed of the wide-gap alloy (9). (The active region is mostly on the p-side of a junction, because the mobility of injected electrons is much higher than that of injected holes.) Thus, the desired structure has an n-type GaAs substrate (or grown layer), an n-type $Al_xGa_{1-x}As$ layer, a p-type active layer, a p-type $Al_yGa_{1-y}As$ layer, and finally a p-type GaAs

layer to facilitate metal contacting.

It is this double-heterojunction structure that has produced room temperature CW lasing, with threshold current below 1000 amps/cm^2, for total internal reflection devices (Alferov et al (10), Panish, Sumski, and Hayashi (11), Selway and Goodwin (12)). A report by Alferov et al (13) of a 600 amp/cm^2 threshold for a Fabry-Perot device may be a misprint.

The aim of this project was to develop procedures for the consistent fabrication of double heterostructures having minimum threshold. Two growth techniques were investigated, the Panish "rigid slider" method (11) and the Woodall isothermal solution mixing (ISM) method (14).

The principal difficulty was in growing an active layer thin enough; threshold is proportional to active layer thickness, down to an optimum thickness which has been found to be about 0.2 μ (12).

The Panish approach, described below, has been reported on more frequently in the literature. It is the one used to produce the very thin layers and low thresholds to date. The Woodall technique was developed with "superlattice" structures in mind (14,15,16), but as will be described below, it holds the promise of a new type of heterostructure having interesting properties.

Note on Liquid Epitaxy

The compositions of the melts and the temperatures of growth were based on published data (17,18,19,20,21,22). For each melt, polycrystalline GaAs (with negligible (10^{16}) n-type doping) was added to liquid gallium in an amount calculated to produce a saturated liquid melt at a (liquidus) temperature 2° - 5^oC above the intended growth temperature (Fig. 1(a)). That is, at the growth temperature the gallium-rich solution contains a small amount of excess solid GaAs.

Aluminum was added to the first and third melts in a quantity that would result in the growth of $Al_xGa_{1-x}As$ alloy with $x \simeq 0.4$ (Fig. 1(b)). The presence of aluminum greatly diminishes the solubility of gallium arsenide in the melt, so the amount of GaAs in these melts was reduced accordinly (18,21) (Fig. 1(c)).

As noted by Panish and Sumski (18) and others, the GaAs does not exist in equilibrium with the Ga-Al-As melt, but rather is coated by a "protective" layer of $Al_xGa_{1-x}As$ at the solution's liquidus temperature. The "x" of this solid alloy coating corresponds to the solidus composition of material which would be grown at that temperature.

The concentrations of the dopants in the melts were selected following Miller et al (17), with reference to papers by Panish et al (23) and Rosztoczy et al (24). For the first melt, tellurium (n-type dopant in GaAs) was chosen; for the second melt, silicon (compensated p); and for the third and fourth, germanium (p).

Two mechanisms of epitaxial growth were investigated. One mechanism is based on the fact that a crystalline layer grows on the surface of a solid in contact with a saturated liquid when the system is cooled while below the liquidus temperature. The thickness of the layer varies directly as the duration of the cooling and as the temperature, and inversely as the rate of cooling. This is the common way of growing epitaxial layers.

The other mechanism, recently proposed and advanced by Woodall, involves mixing two saturated solutions in contact with a substrate. If the solutions have different compositons (for example, in the present case, different amounts of aluminum), but are both saturated at the temperature at which they are mixed, then the mixture is supersaturated

at that temperature (see the phase diagram of isotherms in (14)). This condition is relieved by crystallization of the solute. A layer whose thickness depends on the composition and relative volumes of the two solutions, as well as on the temperature, is thus grown on the substrate.

It should be noted that in both types of growth, the amount of material deposited on the substrate varies inversely as the surface area of alternate growth surfaces (i.e., excess polycrystalline gallium arsenide) (25).

If the temperature of the system is above the liquidus, the substrate will be dissolved away until the composition of the melt becomes such that its liquidus is just the ambient temperature. Of course, if any of the solids in the melt are covered with oxide or grease, they may not dissolve and the melt will not have the planned composition.

The pyrolytic-coated carbon apparatus is shown in Fig. 2.(In the later parts of the work, the centre four wells of a six inch long, six well apparatus were used).

A substrate could be moved from one melt to the next by pushing the slider rod containing it a specified distance. The rods were manufactured with substrate wells of different depths, from 0.25 mm to 2.0 mm. The melt-well container fits into the outer carbon container so that the slider rod slides through it. (The six-well system was designed with the melt-well container resting on the slider rod, to specify precisely the clearance over the substrate as it passes between melts). Although the melt components were chosen to be non-volatile, another slider rod was placed over the melts, and small amounts of deposit were frequently found on this rod directly above the melts.

Each set of carbonware was cleaned between runs by flushing with H_2 and HCl gas at about $900^{\circ}C$ for 1½ hours, then heating to about $1050^{\circ}C$ with no HCl flow for one hour.

With the melt components and substrate loaded, and the slider properly positioned, the apparatus was put into a quartz furnace tube of diameter 2 inches. Due to a quartz stop and guides in the furnace cavity and a stop in the furnace tube, the carbonware could be accurately relocated in the tube and the tube in the furnace.

The furnace tube was built so that gas could be passed through it, entering the tube proper at one end and leaving at the other, near the fitting outside the furnace. Thus, the gas flow was from the region of the melt toward the fitting.

The end of the furnace tube was sealed by a fitting having two joints through which ¼-inch quartz rods could slide. One rod was fitted with a hook which was inserted into one of the melt wells, holding the apparatus firmly in place. This rod, being hollow, contained a chromel-alumel thermocouple which was used to monitor the temperature near the melts. Due either to instabilities in the thermocouple or digital voltmeter, or to rapid fluctuations in temperature caused by the flow of gas around the carbonware, the indicated temperature could be read only with an uncertainty of ± .05 mV, or $\pm 1/8^{\circ}C$. At first, this thermocouple was also used by the furnace power controller; later, for the sake of furnace responsiveness, and to minimize dynamic temperature variations, a separate thermocouple in a well adjacent to the furnace windings was connected to the controller.

The other ¼ inch rod was used to push the carbon slider rod

containing the substrate. After the joint was loosened slightly, the quartz rod could be pushed into the furnace tube a measured distance with negligible gas (or air) leakage.

MATERIALS

The flush gas was palladium-diffused, high purity hydrogen. The gallium was Johnson Matthey Chemicals Ltd. grade A1. The polycrystalline gallium arsenide was negligibly n-doped (10^{16}); the germanium dopant was either intrinsic or negligibly anitomy-doped (10^{16}). The silicon dopant was usually n-type, occasionally p-type, but had a resistivity of 750-1250 Ω cm in either case. The Tellurium was 6N pure.

The substrates were (100), Te doped (3×10^{17}) for the double heterostructure runs, and (111), Cr doped (semi-insulating) for the single-layer runs.

PRELIMINARY INVESTIGATION: Single grown layers (with a quench melt).

At the beginning of the project, a number of runs were carried out in which only one layer was grown, by the ISM technique, on the (111) Ga-surface of a semi-insulating Cr-doped substrate. This was partly for the purpose of gaining experience with the equipment, but there was also the intention of investigating the thicknesses and compositions of layers grown from melts of different aluminum concentrations.

Six different Al concentrations were used: 0.25 a/o, 0.5 a/o, 1.0 a/o, 1.5 a/o and 2.0 a/o. The growth melts comprised 5 gm. of gallium and 2 mg of tellurium, together with appropriate amounts of Al and enough GaAs to saturate the solution with arsenic (see "Note on Liquid Epitaxy")

The components were dissolved during an hour at 880°C. The substrate was pushed into the growth melt and left for 5-10 minutes to equilibrate. The layer was grown from 840° to 820°.

The substrate was then pushed into a quench melt (26) consisting of 2 gm. Ga and 0.2 gm Al. The effect of this melt was as follows. The substrates were 0.25 mm thick, while the slider well was 2.0 mm deep, so there was carried over into the quench melt a volume of growth melt covering the substrate. The arsenic solubility of the quench melt was greatly reduced by the presence of the aluminum and virtually no growth at all took place from the mixed melt. The growth that did occur, $Al_xGa_{1-x}As$ with $x \simeq 1$, readily oxidized and the oxide could be removed with warm dilute HCl.

After the growth, the wafers were investigated by cleaning and etching for 5-10 minutes in a 3 H_2O : 1 HNO_3 solution (this stain did not show up the layers very well). Further, some of the wafers were angle-lapped at about 1° or 3° and etched in 4 H_2O : 3 HNO_3 : 1 HF, which showed up the layers quite well. (Fig. 3). Photoluminescence measurements were made at several points along the bevelled surface.

Aside from experimental results, a number of things were learned in the course of this work. The first concerned the difficulty of mechanically or chemically polishing the (111) - Ga face of the substrate to a flat finish. Best results were obtained by lapping with 5μ aluminum oxide abrasive, then with a ¼ -μ diamond lapping wheel, and finally polishing with a solution of H_2O_2 and NH_4OH ($pH \simeq 7.5$) (27) on a Politex Supreme PS polishing cloth.

The surface at this point would be virtually featureless, but the 4 H_2O : 3 HNO_3 : 1 HF etch prior to loading into the carbonware left triangular pits. Other etches were worse - the problems of etching the Ga - (111) face are well documented (27,28,29). It is to be recommended that growth on this face be preceded by an etch-back in the melt (raising

the temperature of the substrate and melt in equilibrium.)

In general, the As - ($\bar{1}\bar{1}\bar{1}$) face or the (100) face are more convenient for the epitaxial growth; the Ga - (111) face has the added disadvantage that its surface structure is distorted from the bulk structure. (This is because the gallium atoms have insufficient electrons to fill the dangling bonds at the surface, while the group V arsenic atoms, with five valence electrons each, can fill them (29,p.446-7)). The resulting grown surfaces had numerous triangular pits pointing in the <110> direction.

Another thing that was learned at this early stage was that too high a rate of cooling produces uneven growth and a poor surface. Since growth per degree of cooling depends on the rate of cooling, and the layers of different runs were grown with much different cooling rates, it was not possible to compare meaningfully the resulting layers.

Photoluminescence measurements performed on one properly grown wafer lapped at 3° gave a peak in the substrate at 8700-8750 Å, corresponding to an energy transition of 1.42 eV. (the energy gap of GaAs according to published values (8) is 1.43 eV. at room temperature). At the position of apparent maximum aluminum concentration in the grown layer, a peak was observed at 6880 Å, corresponding to a band gap of 1.80 eV. This indicates a concentration of aluminum of about 35% (18); the layer was grown from a solution with 0.25 a/o Al, so the result is in excellent agreement with Rado et al (30). See Fig. 1(b).

(Further support of Rado's data was subsequently obtained from photoluminescence measurements on a bevelled piece of one of the double heterostructure wafers. Emission from the first grown alloy layer, the only one broad enough to subtend the focussed spot of the activating laser, showed clearly a peak at 6930 Å, as well as one at 8730 Å due to the

substrate below the epi layer.)

At this point the furnace was found to have a poor temperature profile, which partly explained the variation in growth of the other layers. The agreement with published work just mentioned supported a decision not to repeat the single-layer runs, but rather to rely on the data of Rado et al, and on that of other published work (17,18,19) which showed that the addition of aluminum to a melt, by reducing the GaAs solubility, slows the growth rate. In view of the limited time available, it was decided to move on to the fabrication of double heterostructures after correcting the furnace profile. The suitability of this plan was confirmed when satisfactory multilayers were subsequently grown.

Development of a Double Heterostructure Laser

The work concentrated on the compositions and thicknesses of the epitaxial layers, bearing in mind the following requirements of double heterostructure lasers:

1. Active layer thickness was to be minimized, aiming at 0.2 μ.
2. Barrier layers were to have about 40 a/o Al As.
3. The thicknesses of the first and third layers had to be greater than the wavelength of the light produced in order to have good waveguiding. (inside the material, which has refractive index 3.4, the wavelength is about 0.25 μ).
4. Ideally, the total thickness of the third and fourth layers should be ≤ 2 μ, to satisfy heat-sinking requirements.

The Procedure

The melt compositions were as shown in Fig. 4. All but the gallium were taken from quantities which were degreased, etched periodically, and

stored in air in covered beakers.

For the Panish method, the backside of the substrate was lapped to 0.21-0.24 mm. (.0085" - .0095") with 5 μ aluminum oxide abrasive; for the ISM method, the substrate was left 0.40 mm thick. In either case, the substrate was then degreased by boiling in trichlorethylene.

Just before loading the substrate into the carbonware, it was etched for 30-60 sec. in 4 H_2O : 3 HNO_3 : 1 HF. (It is to be noted that a brown film sometimes appeared on the surface of the substrate after etching; this film was avoided if there was not so much agitation during the etching that the oxide formed by the nitric acid could not be entirely removed by the hydrofluoric). The substrate was then rinsed and stored in acetone and dried with a nitrogen blower immediately prior to loading in order to minimize oxidation by the atmosphere. Finally, the substrate was placed in the well (0.25 mm deep for the Panish technique, 0.75 mm or more for the ISM technique) of a slider rod.

The rod was then positioned in the melt holder and the solid components of each melt were followed into the wells by liquid gallium. The loaded carbonware was placed in the furnace tube, which was put into a fixed, relocatable position in the furnace.

It was hoped that this procedure prevented excessive oxidation of the substrate between the etch and immersion in a hydrogen atmosphere. It was recognized that the materials might better have been stored, and the loading performed, in a nitrogen-blown drybox, but one was not available.

When loaded, the furnace was heated to 890°C, left for an hour to dissolve the melt materials, and cooled to 850°C. The substrate was pushed into contact with the first melt, left to equilibrate for 15 minutes, and etched back by a 3° rise in temperature.

The first layer was grown at a rate of ½°C per minute for 10°-12°. For the Panish runs, this rate of cooling was continued while the wafer was pushed into the other melts, and left in each for a time interval dependent on the layer thickness desired.

For the ISM runs, the temperature was stabilized before the wafer was moved into the second (active layer) melt. After two minutes, more than enough for complete ISM growth (14), the wafer was pushed into the third melt for another two minutes at the same temperature. Then the third layer was sometimes made thicker by cooling growth and the fourth melt was used to grow the final layer by either mechanism or both. Finally, the growth was sometimes quenched as described earlier. (Thus, the ISM runs actually represented a hybrid procedure.)

At first, five hours or more were taken to cool the carbonware back to room temperature, but later the tube was gradually pulled out of the furnace and the time was reduced to about 45 minutes. Flushing with hydrogen was continued at least down to 300°C.

Characterization

When the layers had been grown and the apparatus cooled, the wafer was examined as follows.

First, any gallium clinging to the surface was removed either by wiping gently with a cotton swab dipped in warm dilute hydrochloric acid, or by washing with a fine brush in warm water with a small amount of "Sparkleen" detergent added. The warm water and detergent were found to work better, although a vigourous and potentially damaging reaction was observed if the detergent solution was too concentrated.

The wafer was rinsed in water then methanol or acetone for fast drying. After ISM runs, it would be .016" or .017" thick, and had to be

lapped (with 5 μ Al oxide abrasive) to .080" or less for easy cleaving (which would expose (110) faces). After Panish-method runs, the .085" - .095" thick wafer was cleaved without further lapping, but severe strain or fracture lines appeared on the face of the cleave.

After the cleaving, one of the pieces was stained by an etch of five minutes or longer in dilute nitric acid. The cleaved edge was then inspected and photographed under a microscope (X560 magnification) with Nomarski interference contrast. The thicknesses of the layers were measured with a filar micrometer eyepiece on the microscope.

Chips were cleaved from this piece of the wafer, and a transistor-curve tracer was used to check immediately on the light-emitting diode character of the structure. The light was observed with a hand-held infrared viewer and an idea of the localization of the emission was obtained by viewing the chips with the viewer through a low-power microscope.

If the wafer looked promising, a large piece of it was carefully lapped down to about .004", deoxidized, and given metal contacts by evaporating a layer (∿2μ thick) of gold on each surface. It was then broken up and parts were sawn into strips .003" - .004" wide. The strips were cleaved into lengths of .008" to .018". These mesa chips were mounted as lasers, either on headers (Fig. 5) or by pressure bonding on copper heat sinks, and their lasing properties were investigated.

Other pieces of the wafer were mounted on headers with silver paste. They were viewed in a scanning electron microscope under voltage contrast, biased and unbiased. The purposes of this were to better view the layer thicknesses (utilizing the high magnification of the SEM), and to find the effective location of the electrical junction (for which the beam-

induced current technique was also tried; when the electron beam hits near the electrical junction on the edge of the chip diode, a current is produced across it). Unfortunately, insufficient voltage differences could be produced between adjacent layers, at reasonable currents, to make the layers very much clearer than they were when viewed optically.

To locate the effective junction, these mounted pieces were also studied under an infrared microscope (X200 magnification). However, the resolution in the infrared did not permit inspection of layers about 1 μ thick.

Two additional methods of characterization were considered but there was insufficient time to apply them. They are to be recommended for investigation.

The first of these was the observation of the "breakpoint" in the curve $\frac{dV}{dI}$ vs I (values taken from the I-V characteristic). As reported by Rode and Dawson (31), there is a firm relationship between the (high) current at this breakpoint and the threshold for lasing: the breakpoint occurs at currents 30% below the lasing threshold, even when the (Fabry - Perot) laser mirrors are destroyed. This implies that it may be possible to predict thresholds without going through the process of mounting (i.e. heat sinking) chips as lasers. (Some heat sinking would still be necessary, since at currents 70% of threshold, a lot of power is being dissipated).

The other method involved constructing an apparatus which would apply a metal surface of known area to the surface of the wafer. The carrier level (i.e. doping concentration) near the surface of the wafer may be calculated from the capacitance-voltage characteristic of the resulting Schottky barrier (32):

$$N_D = \frac{2}{qE_s} \left(- \frac{dV}{d(^1/_{C^2})} \right) .$$

By etching the wafer a number of times and observing the voltage and capacitance between etches, the doping profile across the heterostructure layers can be determined. Note that the Schottky barrier depletion layer width increases with voltage, a fact that reduces the number of etches necessary to obtain a well-mapped profile.

A suitable apparatus was constructed, but the complications in the analysis of the measurements, pointed out by Severin and Poodt (33), as well as the shortage of time, discouraged its implementation.

Results of Double Heterostructure Fabrication.

1. Laser Performance

Data on the most significant of the runs are itemized in Fig. 6.

The first three runs were of the isothermal solution mixing type. Their purpose was to determine the relationship between volume of carryover melt and layer thickness. In fact, the thickness of the grown layer is in inverse proportion to the area of the substrate, (the area of the bottom of the substrate well) ignoring the small amount of growth on the bits of excess GaAs in the melt. Therefore, a convenient and meaningful variable is the depth of the melt carryover in the substrate well, rather than the volume.

The visibility of the layers of ISM-B1 under the microscopes was poor; it is likely that the effect of isothermal growth was countered by melt back associated with a slow $\frac{1}{4}^{\circ}$ rise in temperature while the substrate was in the active layer melt. The short wavelength of the emitted laser

radiation, ∿ 7900 Å, suggests that only a partial decrease in Al concentration near the electrical junction was produced; that is, there was almost a homostructure in $Al_xGa_{1-x}As$, with correspondingly poor carrier confinement.

Later, these ISM runs were repeated, but only the repeat of ISM-B1, called ISM-B10, was comparable to the original because of the misbehavior of the furnace, described elsewhere. Due to this misbehavior, the control of all variables in successive runs may be suspect, but the results do confirm the expected relationship between layer thickness and carryover depth, and indicate the form of that relationship (Fig. 7).

The wafer TLS-B2, only the second one fabricated by the conventional cooling technique, had flat, uniform layers and produced excellent laser chips with thresholds approaching the lowest obtained in the course of the work, 3.7-4.3 kA/cm^2.

The pictures of the stained edges of ISM-B4 and TLS-B8 are good examples of what LPE layers look like (Fig. 8); grown by different methods, they both show how straight and parallel are the grown layers. (The differences in apparent contrasts of the layers in the two photographs must be ascribed to the setting of the Nomarski attachment on the microscope, or to the temperature of the stain etch (3 H_2O : 1 HNO_3 in each case)).

The thresholds of the chips from TLS-B8 were not very low (even allowing that longer chips would be expected to have lower thresholds (12)), but this is explained by the active layer thickness, 1.6 μ. The chips from ISM-B4, on the other hand, had thresholds which were quite low and definitely encouraged the continued exploration of this technique.

ISM-B14 was grown in an unpredictable furnace, but reasonable

thresholds were measured in chips from some parts of the sample. Chips from other places in the wafer had higher thresholds or did not lase at all. This shows that although lasing structures can be obtained with relative ease by liquid epitaxy, it is another matter to produce a uniform DH wafer with a high yield of laser chips.

The growth of TLS-B22 was also very non-uniform; an optical picture of a cleaved edge at one place in the wafer clearly shows an active layer 2.2 μ wide, while an electron micrograph of a laser chip shows a 0.46 μ active layer. The chips having been selected fortuitously from a "good" area of the wafer, fairly low thresholds (3.7, 5.3 kA/cm^2) were obtained from rather short chips.

There were only three layers visible where the optical micrograph of ISM-B25 was taken; either there was no active layer at that place in the wafer or it was too thin to be seen with the resolution of the optical microscope. The laser chips however, had good active layers, for although the thresholds were not very low, their external quantum efficiencies were measured to be about 10% (137 mW/amp). The linearity of the current-power output characteristic (I-L curve) may be seen in Fig. 9. An efficiency of 10% is comparable to that of commercially available lasers.

The best results, in terms of threshold, efficiency, and power, were obtained from ISM-B26 and ISM-B27. A chip from ISM-B26, with a threshold of only 2.76 kA/cm^2, put out 1 Watt of light at 5 Amps current, and had external efficiency of about 18.5%. The performance of ISM-B27 was not quite up to these standards, but the fact that three chips had low thresholds (3.1-3.3 kA/cm^2), efficiencies on the order of 14%, and reasonable power output (675 mW @ 5A for one, 425 mW at 2A for another), represents both consistency and high performance from this wafer.

Attempts to operate the chips CW failed when the sub-threshold luminous efficiencies fell due to overheating as the threshold current was approached. The failure was caused by poor heat sinking: the chips were only pressure-bonded to copper studs, and their surfaces were not flat enough to give good thermal contact.

From the temperature records during these growth runs, it is apparent that there were no spurious temperature fluctuations, and that the active layers were definitely grown by isothermal solution mixing. The performance of these chips, with respect to threshold and to efficiency and power output, is much better than any previously reported for ISM-grown devices (14).

One of the wafers, ISM-B4, which had particularly visible layers (Fig. 8) was supplied with current and the edge was viewed under an infrared microscope. The 1 μ active layer could not be discerned, and the first visible light appeared as a line of indeterminate width (but approximately the active layer width), running the length of the sample, implying a very uniform active layer. This light became visible at about 6 mA. At higher current levels, the light emission took on the appearance of a band, spreading through the n-side $Al_xGa_{1-x}As$ barrier. The p-side barrier was much narrower, but since it is the transparency of the alloy to the recombination radiation that results in the spreading, it is obvious that the effect will be much reduced in extent on the p-side of the junction. Pictures taken in the infrared of the edge of the wafer at several currents levels (Fig. 10) show that the breadth of the band is limited by the boundary between the substrate and the first grown (alloy) layer.

The diffused appearance of the spontaneous emission should be contrasted with the narrow confinement of the stimulated emission, in which stationary filaments of high-intensity emission were observed.

2. Spectroanalysis

The light emitted by pieces cleaved from several of the ISM wafers was spectroanalyzed by means of a Spex 1702 spectrometer and a strip-chart recorder. The data is presented in Fig. 11.

A number of specific transitions were identified, allowing for a ± 50 Å uncertainty and the shift of peaks to longer wavelengths at higher currents (caused by the temperature rise at high power levels which decreases the band gap). It is known that the silicon dopant in GaAs (band gap 1.44 eV at 300°K) produces two acceptor levels, with activation energies of 0.03 eV and 0.1 eV, and one shallow donor (34). The recombination transitions of 1.44 eV, 1.41 eV, and 1.34 eV are associated with emitted radiation of wavelengths, 9620 Å, 8800 Å, and 9250 Å respectively. Lasing usually occurs among these wavelengths, the exact emission energy (peak) depending on the amount of Al in the active region.

The spectrum for ISM-B2 was closely related to recombination on the 0.1 eV Si level, with little or no Al in the active region, and in ISM-B3 the two Si acceptor levels appeared to be competing, the level nearer the valence band dominating at higher currents. The spectra of three of the pieces of ISM-B4 were dominated by the 0.1 eV Si level, while the other two were shown to have active regions with some aluminum contamination and a consequently larger band gap.

At all currents, ISM-B25 shows evidence of transitions across the GaAs band gap (the 8530 Å radiation), and the 0.1 eV Si level is exhibited at high current levels. In addition, at 200 mA of current a significant proportion of the recombination of is apparently occuring just outside the GaAs layer proper, and the radiation spectrum contains peaks of several shorter wavelengths.

The spectrum from ISM-B26 was probably dominated once again by the 0.1 eV Si level in an active layer whose band gap was broadened by the presence of Al. ISM-B27 produced a peak corresponding to the band gap of GaAs with no Al, and a "shoulder" on the side of this peak that would represent recombination on the 0.1 eV Si acceptor.

Thus, the ISM-grown active layers usually had noticeable aluminum in them, as would be expected from a growth method that mixes an alloy melt with the GaAs active layer melt. There was emission characteristic of recombination on the Si acceptor levels, particularly the one 1.34 eV below the conduction band. Also, there was some emission from near the alloy heterojunctions at high currents, indicated by the appearance of shorter wavelength peaks.

Summary

In the course of this work gallium aluminum arsenide double heterostructures were grown using both an established procedure (cooling growth) and a relatively unexplored method (isothermal solution mixing). The aluminum concentrations of the epitaxial layers were found to be predictable, and while the impurity concentration profiles were not mapped, the performance of the laser diodes indicates that doping levels were not far from those anticipated. It was not difficult to get layer thicknesses down to 0.4-0.5μ, but to reach the optimum active layer thickness of 0.2 μ will take further refinement of the procedure, and possibly of the equipment. (It may be noted in this respect that because GaAs layers grow more quickly than aluminum alloy layers, the former, including the active layer, are more difficult to grow thin than are the latter).

The performance of many of the devices produced, while not state-of-the-art, was quite close to the requirements for a CW room temperature laser (aside from longevity). Although continuous mode operation was not achieved, the

current thresholds were very near the values necessary. The external quantum efficiency of ISM-B26 was, at 18.5%, quite reasonable.

One anomaly in the results was the fact that TLS-B2 had an active layer of uniform thickness about 1.1 μ, while the other wafers with thinner uniform active layers nevertheless had higher thresholds. This may be explained by means of more sophisticated characterization, especially with regard to crystal structure quality, unintended impurity contamination and compositional homogeneity within each layer; or it may be due to inconsistencies in chip fabrication after growth. For example, current leakage would cause a higher observed threshold, and a sawn surface is notoriously leaky. Also, when the chips were pressure bonded to the copper studs, some were fractured because their surfaces were not smooth enough; it is possible that cracks in others were not subsequently detected, and thus the laser diodes were made lossy, or the actual length of the lasing part of the chip was so short as to cause a high threshold (12). In any event, the pressure bonding may cause stress on the chips that results in non-radiative recombination centres along lines of crystal dislocation (See Fig. 12). Gentler methods of preparing the chips as lasers would be recommended (35).

In general, though, the ease with which the laser results were obtained is encouraging with regard to production of operable CW-mode lasers.

Recommendations

1. Furnace behaviour

The chief difficulty in this work was getting consistent, stable performance from the furnaces. Much time was spent measuring and adjusting temperature profiles and a number of runs were spoiled by unpredictable furnace behaviour.

After the single layer runs (see below) but before the commencement of the multilayer growth investigation, the temperature profile of the 2998 furnace was mapped and found unacceptable, a fact which helps to explain the unsatisfactory results to that point. Heating coils of the furnace were then shunted so that there was only a 1°C variation in temperature over the melt positions, as measured by a thermocouple in a quartz tube running alongside the carbonware. It was assumed in this profiling that the temperature variations within the carbonware would be reduced by the high thermal conductivity of the carbon.

When the multilayer runs began giving poor results, the profile of the furnace was rechecked, and it was found to be longer flat. Further shunting adjustments could not restore a good profile, so the work was carried on in the 1137 furnace. Because it was shorter and had a larger bore, the 1137 profile was difficult to flatten, and because it was a new furnace, the profile was unstable from run to run, even after a thorough running-in.

It is recommended that work of this multiwell-slider type be performed in a long furnace with a high length-to-bore ratio. (like the model 2998) using a carbon apparatus whose melt wells are closer together Alternatively, an apparatus could be designed in which a substrate in a well in a rotating disc is moved through melt wells arranged cylindrically. Such an apparatus, to be used with the furnace set up vertically, would leave the substrate at the same vertical position, and at the same radial position in the furnace cavity as well, obviating the need for a long temperature-flat zone. In addition, by locating the apparatus suitably in the furnace, almost any desired temperature gradient between the substrate and the melt above it may be easily obtained.

2. An improved heterostructure.

In a patent application (35) Hayashi describes what he calls a double double heterostructure (DDH) laser. This structure has a narrow GaAs "electrically active" region in the centre of a broader region acting as an optical cavity (37).

Carrier recombination (and hence optical gain) is confined to the inner active region (whose optimum thickness may be even less than 0.2 μ) by a potential step whose height is not sufficient to confine the light. The light is confined by another pair of heterojunctions, which form the waveguide.

The confinement of the carriers produces high gain and low thresholds, while the spreading of the optical field reduces power density, thus increasing power-handling capacity. Further, the interaction between the carriers and the optical field, concentrated near the centre of that field, tends to suppress higher order modes, permitting high-power, fundamental mode operations.

The same dual effect of the DDH structure might be obtained in a device whose layers were grown by isothermal solution mixing. In the Panish slider technique, each layer is grown from a different melt, ideally with all the previous melt wiped off the surface of the substrate by the wall between the wells. This results in a relatively abrupt junctions between layers ((38), but see also (39)), and flat composition profiles across at least the narrow layers. Growth by the ISM method, on the other hand, results in a layer structure with much more graded junctions because growth occurs while the composition of the mixed solution is changing, moving towards equilibrium.

Thus, the active layer of an ISM-grown device would be expected to have a U-shaped, rather than a "square-well", composition profile. Hayashi's

DDH device has a stepped, U-shaped profile. This similarity between the two structures suggests that the "gradual" double heterostructure grown isothermally might confine the light to a wider region than that to which the carrier injection would be confined and its performance might resemble that of the discrete DDH.

Even if this turns out not to be the case, the performance, in terms of threshold and efficiency, of the chips grown by the ISM method in the present work shows the promise the technique holds for the fabrication of heterostructure lasers. Since melt composition is more easily controlled and monitored than are temperature gradients and cooling rates, further development is certainly in order.

Note added in proof:

Further development in chip preparation techniques, carried out as this report was written, has resulted in almost CW operation of a chip from ISM-B26.

The chip was pressed with minimum force onto a copper stud covered with a thin layer of molten solder. The resultant heat sinking was good enough to allow the application of a current above threshold (800 mA, $\sim$ 2.7 kA/cm^2), with approximately a 70% duty cycle (from a transistor-curve tracer).

The lasing produced at the onset of a pulse was soon quenched by heating effects. However, later inspection revealed that while the solder was in contact with the surface of the chip, it did not actually wet the whole surface.

This indicates that there are still considerable improvements in laser performance to be realized simply through better heat-sinking. It is clear that chips already produced are capable of lasing continuously.

BIBLIOGRAPHY

1. (a) R.N. Hall, et al, Phys. Rev. Lett. 9, 366 (1962)
   (b) M.I. Nathan, et al, Appl. Phys. Lett 1, 62 (1962)
   (c) T.M. Quist, et al, Appl. Phys. Lett 1, 91 (1962)

2. I. Hayashi, M.B. Panish, P.W. Foy, S. Sunski, Appl. Phys. Lett. 17, #3, 109-111 (1 Aug. 1970).

3. H. Kroemer, Proc. IEEE, 1782 (1963).

4. Hayashi, Panish, Foy, IEEE J. of Quant. Electron. 5, 211-2 (1969).

5. H. Kressel and H. Nelson, RCA Rev. 30, 106-113 (1969).

6. Goodwin and Selway, IEEE J. of Quant. Electron. 6, 285-290 (1970).

7. W. Kischio, Z. onorg. allg. Chem. 328, 187 (1964)
   R.A. Ruehrwein, Deutche Auslegschrift DAS 1132098.

8. M.D. Sturge, Phys. Rev. 127, 768 (1962).

9. Zh. I. Alferov, V.M. Andrew, E.L. Portnoir, M.K. Trukan, Sov. Phys. - Semic. 3, 1107-10 (1970).

10. Zh. I. Alferov, V.M. Andrew, E.L. Portnoir, M.K. Trukan, Sov. Phys. - Semicond. 4, 1573-5 (1971).

11. M.B. Panish, S. Sunski, I. Hayashi, Metallurgical Trans. 2, 795-801 (Mar 1971).

12. P.R. Selway, A.R. Goodwin, J. Phys. D:Appl. Phys. 5, 904-914 (1972).

13. Zh. I. Alferov et al, Sov. Phys. - Semiconductors 6, #3, 495 (Sept 1972).

14. J.M. Woodall, J. Electrochem. Soc. Solid Statc Sci. 118, #1, 150-152 (Jan 1971).

15. J.M. Woodall, J. Crystal Growth 12, 32-38 (1972).

16. P. Zory and J. Woodall, IBM Tech. Disclosure Bull. 15, #1, 163 (June 1972).

17. B.I. Miller, E. Pinkas, I. Hayashi, R.J. Capik, J. Appl. Phys. 43, #6, 2817-26 (June 1972).

18. Panish and Sumski, J. Phys. Chem. Solids 30, 129-137 (1969).

19. M. Flegems and G.L. Pearson, Proc. 2nd Inter. Symp. on GaAs, the Institute of Physics and The Physical Society, London, 1968, p.22-27.

20. (a) R.N. Hall, J. Electrochem. Soc. 110, 385 (1963).
(b) E. Andre, J.M. LeDuc, and M. Mahieu, J. Crystal Growth 13/14, p.663-667 (1972).

21. J.N. Woodall, M. Rupprecht, and W. Renter, J. Electrochem. Soc. Electrochem Tech. 116, #6 p.899-903 (June 1969).

22. W.G. Rado, W.J. Johnson, and R.L. Crawley, J. Electrochem. Soc. Sol. St. Sci. & Tech. 119, #5, 652-3 (May 1972).

23. (a) M.B. Panish and S. Sumski, J. Appl. Phys. 41, p.3195-97 (1970).
(b) Panish, J. Electrochem. Soc. 113, #11, 1226-28 (Nov 1966).
(c) Panish, J. Electrochem Soc. Sol. St. Sci. 114, #1, 91-95 (Jan 1967).
(d) Panish, J. Less-Common Metals 10, 416-424 (1966).

24. F.E. Rosztoczy, F. Ermanis, I. Hayashi, and B. Schwartz, J. Apply. Phys. 41, #1, 264-270 (1970).

25. M.F. Lockwood and M. Ettenberg, J. Crystal Growth 15, 81-83 (1972).

26. R.M. Potemski and J.M. Woodall, J. Electrochem Soc. Soc. St. Sci & Tech. 119, #2 277-279 (Feb 1972).

27. J.C. Dyment and G.A. Rozgonyi, J. Electrochem Soc. Sol. St. Sci. 118, #8, 1346-1350 (Aug 1971).

28. J.L. Richards and A.J. Crocker, J. Appl. Phys. 31, 611-12 (1960).

29. "Compound Semiconductors v. 1: Preparation of III-V Compounds", ed. by R.K. Willardson and M.L. Goering, Reinhold Publishing Corp., New York, 1962.

30. W.C. Rado, W.J. Johnson, R.L. Crawley, J. Appl. Phys. 43, #6, 2763-65 (June 1972).

31. D.L. Rode and L.R. Dawson, Appl. Phys. Lett. 21, #3, 70-936 (Aug 1972).

32. "Physics of Semiconductors Devices", by S.M. Sze, Wiley-Interscience, (1969).

33. P.J. Senerin and G.J. Poodt, J. Electrochem. Soc. Sol. St. Sci. & Tech. 119, #10 1384-89 (Oct 1972).

34. H. Kressel, J.U. Dunse, H. Nelson, and G.Z. Hawrylo, J. Appl. Phys. 39, 2006 (1968).

35. Hayashi, Panish, and F.K. Reinhart, J. Appl. Phys. 42, #5, 1929-41 (April 1971).

36. I. Hayashi, Canadian Patent #909395, Sept 5, 1972, granted to Western Electric Co. Inc., New York, U.S.A.

37. H. Kressel et al, RCA Rev. 32, 393-401 (1971).

38. (a) Alferov, Andrew, Kord'kov, Portnoir, and Tret'yokov, Sov. Phys. Semicond. 2, 843 (1969).
(b) Alferov, Andrew, Zimogorova, and Tret'yokov, Sov. Phys. Semicond. 3, 1373 (1970).
(c) R.L. Anderson, Sol. St. Electron. 5, 341 (1962).
McMASTER UNIVERSITY LIBRARY

39. J.F. Womac and R.H. Rediker, J. Appl. Phys. 43, #10, 4129-33 (Oct 1972).

40. J.A. Rossi and J.J. Hsieh, "Double heterostructure GaAs : Si diode lasers", Appl. Phys. Lett. 21, #6, 287-9 (15 Sept 1972).

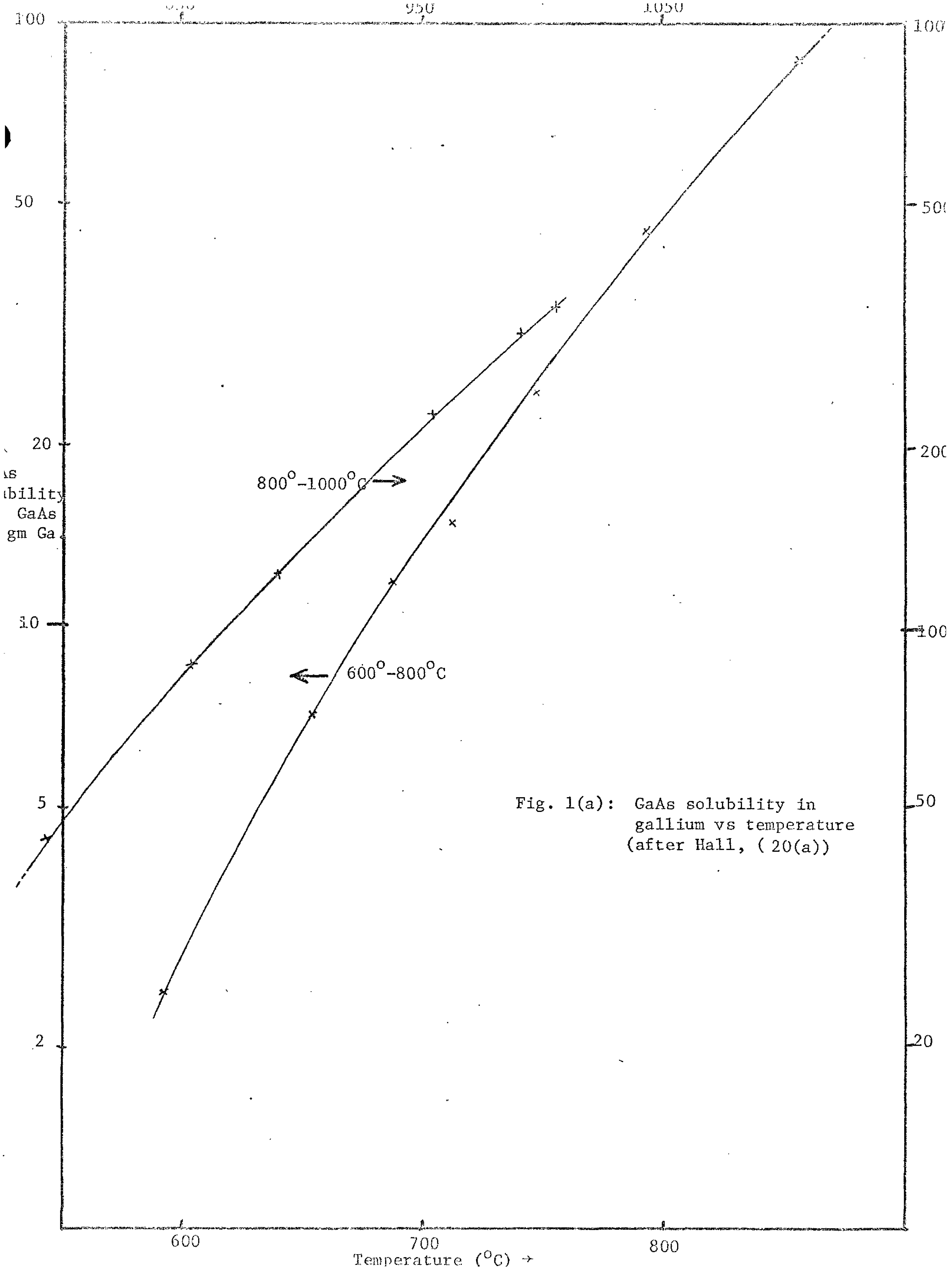

Fig. 1(a): GaAs solubility in gallium vs temperature (after Hall, (20(a))

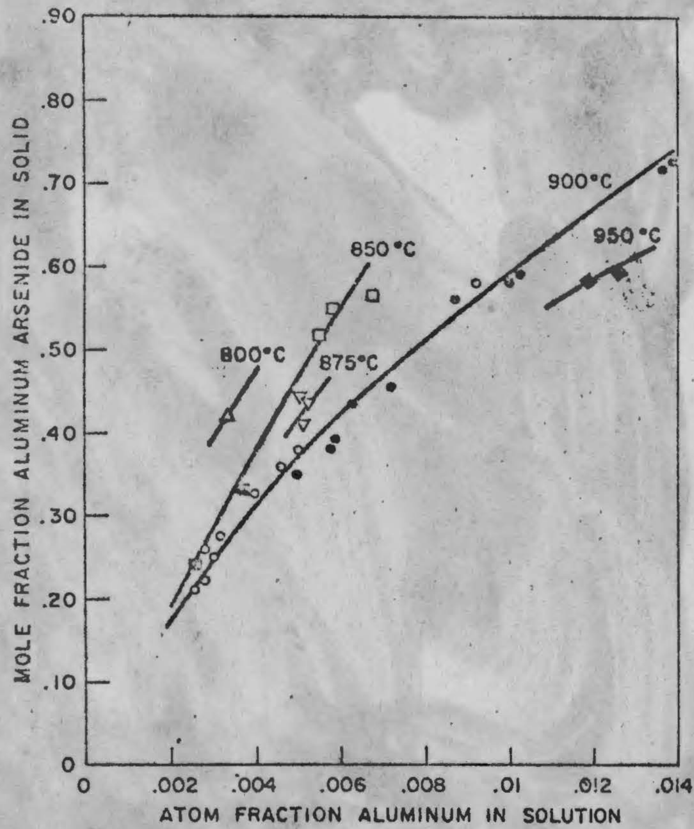

Fig. 1. Initial AlAs concentration in solid $Ga_{1-x}Al_xAs$ vs. Al atom fraction in Ga-Al-As solution for specific values of T_s. For $T_s \neq T_e$, △ 800°-805°C, □ 850°-855°C, ▽ 875°C, ○ 895°-905°C. For $T_s = T_e - 40°C$, ▣ 850°-855°C, ● 895°-905°C, ◆ 945°-950°C.

Rado, Johnson, and Crawley (30) - Fig. 1(b)

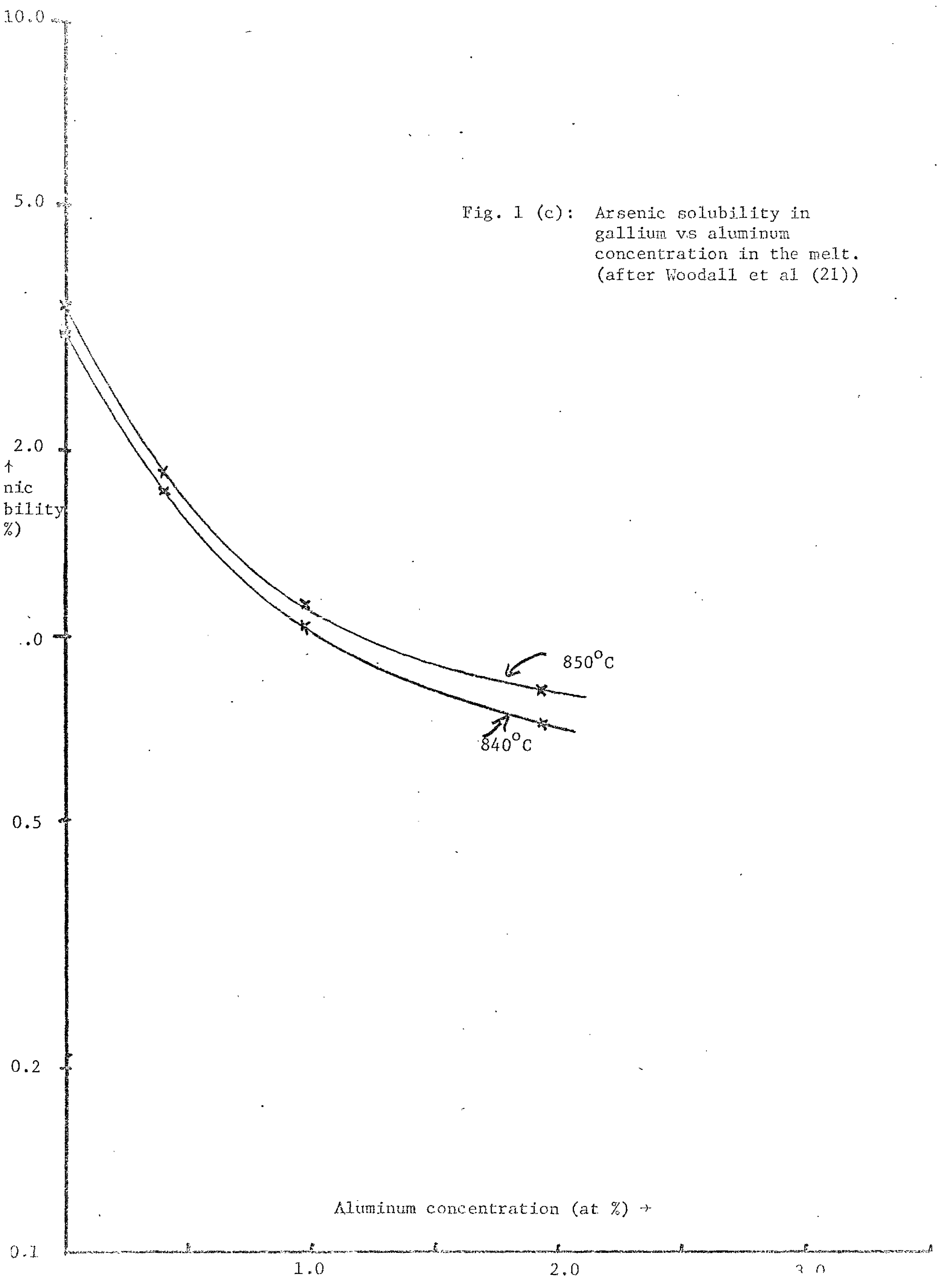

Fig. 1 (c): Arsenic solubility in gallium vs aluminum concentration in the melt. (after Woodall et al (21))

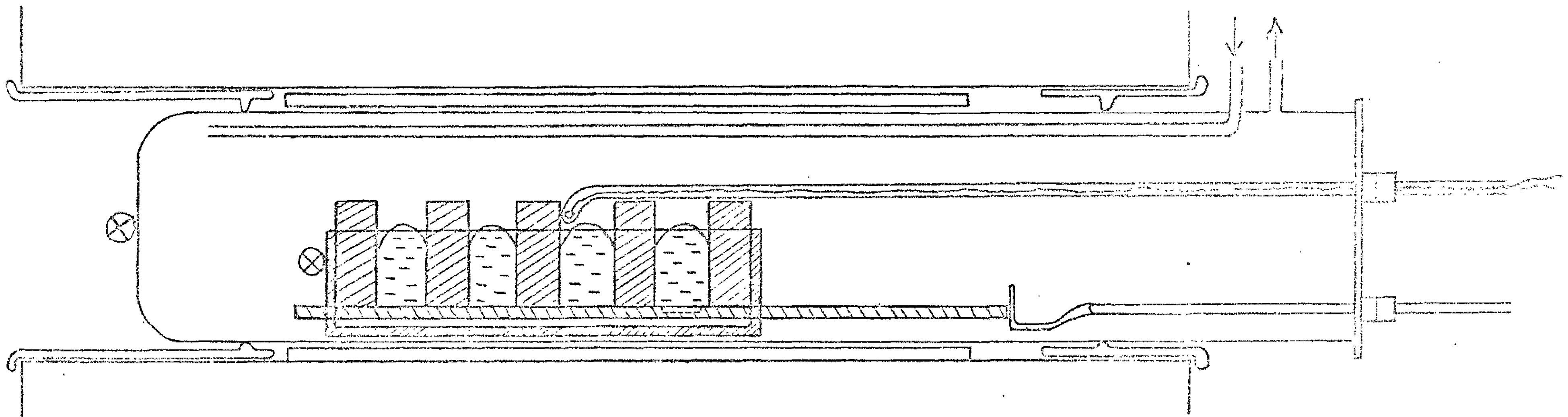

Carbonware with melts, in furnace tube;
showing push rod, thermocouple rod, gas ducts,
fitting with joints, and stops, furnace tube
guide, and Inconel pipe. Not to scale.

Fig. 2

Fig. 3: Single-layer wafer, lapped at 3° and etched in 3 H_2O : 1 HNO_3. Layer thickness ≃ 22μ.

	Ga(gm)	GaAs (mg)	Al (mg)	Doping (mg)	
Melt #1	5	240 (1.85a/o)	8 (.41a/o)	1 (.01a/o)	Te
Melt #2	5	400 (3.1 a/o)	-	30 (1.4a/o)	Si
Melt #3	5	220 (1.72a/o)	8 (.41a/o)	75 (1.4a/o)	Ge
Melt #4	5	400 (3.1a/o)	-	50 (0.9a/o)	Ge
Quench	3	-	400	-	

Fig. 4

Fig. 5: Laser chip mounted p-side up on header, with silver paint.

UN NO	REMARKS ON GROWTH	DESCRIPTION OF LAYERS *	UNIFORM OVER WAFER?	J_{th} at 300°K (kA/cm²)	LASER CHIP SIZE (10^{-3}in)	GENERAL REMARKS
SM-B1	.016" substrate in .080" well. Temp. drifted up .01 mV during active layer growth	#1 = 16μ, #4 = 50μ, <u>#2</u> & #3 hard to see	yes	25 30	17 x 4 17 x 3	lased at 7910±50Å lased at 7930±50Å Switching in I-V characteristic
M-B2	.016" substrate, .060" well. Temp fell .005 mV on moving into each melt, then rose again, except in #2	#1 ≃ 6μ, #4 ≃ 55μ, <u>#2 = 1.25</u> ± <u>.1μ</u>, #3 = .9 ± .1	Apparently visibility varied			Metal contacts didn't "take".
M-B3	.016" substrate, .040" well; constant temp. during #2, #3, and #4	#1 ≃ 9μ, <u>#2 = .76μ</u> #3 ≃ .38μ, #4 ≃ 45μ	Yes	16 15	10 x 3 10 x 3	
S-B2	Temp dropped ∿.025 mV in #2, ∿.025 in #3, .12 in #4	∿10μ, <u>1.06μ</u>, 1.75μ, ∿14 μ.	Yes	12 5 4.3 3.7	14 x 3.25 12.5 x 3 14 x 4 15 x 4	
SM-B4	.017" substrate with .009" wafer under it in .040" well. Temp dropped .01 mV on pushing into #2.	∿12, <u>0.87±.1</u>, 1.2, ∿25μ	yes excellent	7 7 5 6.5	13 x 3 11 x 3 18 x 4.5 37 x 4	See Fig. 8 (a).
S-B8	Held between #1 and #2 for a few sec., but temp fell .01 on going into #2 anyway. In #2 for 5 sec #3 grew for ∿.04 mV.	∿7, <u>1.56</u>, 1.33, 2.5μ	very uniform over most of wafer	14 14.3 14	9.5 x 4 11.5 x 3 9 x 3	See Fig. 8(b).
M-B10	.016" substrate in .080" well. Temp. dropped .005 mV going into each melt.	∿6.5μ, <u>1.50±.2</u>, 1.2±.15, 4.2 μ.	over most of the wafer			Repeats ISM-B1
	* Thicknesses to .01μ were measured on SEM electron micrograph. Underlined values refer to active layer. Final layer thickness is before lapping.					Fig. 6

RUN NO.	REMARKS ON GROWTH	DESCRIPTION OF LAYERS *	UNIFORM OVER WAFER?	J_{th} at 300°K (kA/cm^2)	LASER CHIP SIZE (10^{-3}in)	GENERAL REMARKS
ISM-B14	.016" substrate in .060" well Temp dropped .005 in #2, #3 grew for .065 mV.	∿5.7, 2.6, 1.5, 5.0	No	8.5 10.3 15 14	11 x 3 11 x 2.25 8 x 2.5 11 x 3	(132 mW) (165 mW) Repeats ISM-B. (90 mW)
LS-B22	.0084" substrate in .010" well. Cooling rate ≳½°/in 1'5" in #2, 2"2" in #3, 2"5" in #4.	Optically ∿25, 2.2, 2.7, 2.6μ SEM (laser chip): ∿11, 0.46±.1, 2.3, ∿7μ.	No	5.3 6.6 3.7	11 x 2.5 9.5 x 2.5 13 x 2.5	60 mW at 2A
ISM-B25	.016" substrate in .061" well. 2"5" in #2. Temp went up ∿.01 in #3 before falling for coding growth.	Optically: 25, 0.7, 36 (couldn't see 4 layers)	No, wavy	7.6 7.0 8.8	19 x 2.8 9.5 x 3.8 10 x 3	45 mW @ 5 Amp 450 mW @ 5 Amp 410 mW @ 5 Amp (η_{ext} ~1 (See Fig.9)
ISM-B26	.016" substrate in .040" well. 2'5" in #2. Temp increased .005 mV in #2, .01 in #3.	∿20, 1.5, ∿30μ. Active layer not optically visible.	Yes	3.6 2.76 No Lasing	12 x 3 16.5 x 3.5 11 x 6	90 mW/2 Amp 1 W/5 Amp max(η_{ext}=18.5 CW attempts failed.
SM-B27	.017" substrate in .031 well. 2'5" in #2 Temp increased .01 mV in #3.	∿22μ, 0.7μ, 3.0μ, optically. Only 3 visible.	Yes	3.3 3.3 3.1	16 x 3 11 x 2.25 14.5 x 3.5	675 mW @ 5A (η_{ext}=14%) 425 mW @ 2A CW attempts failed.

Fig. 6 (cont.)

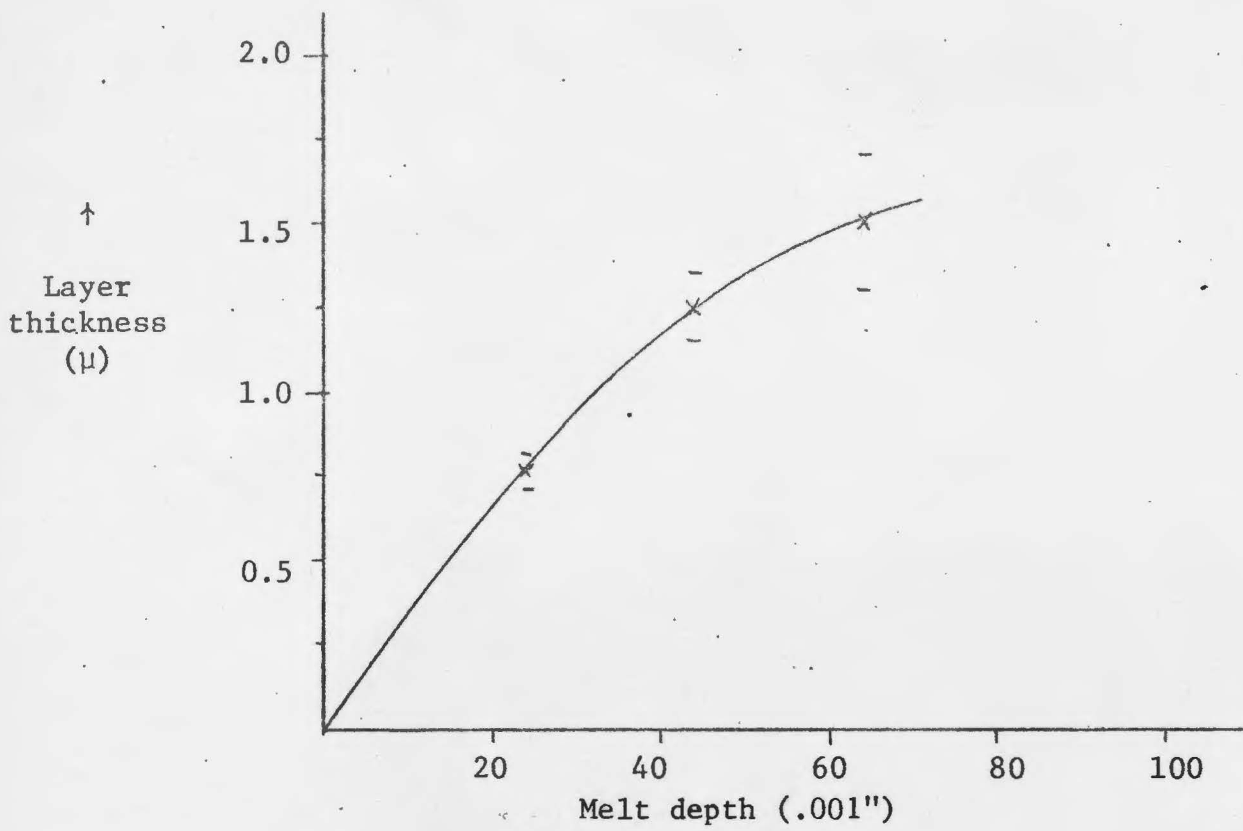

Fig. 7: Graph of thickness of grown active layer vs depth of melt in substrate well.

Fig. 8(a): Cleaved edge of ISM-B4, stained in 3 H_2O : 1 HNO_3 .

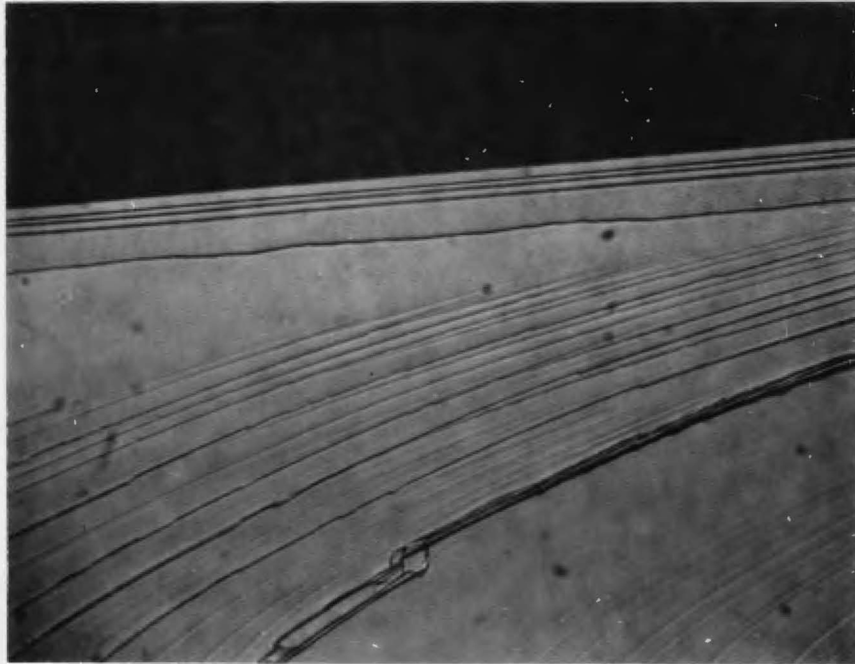

Fig. 8(b): Cleaved edge of TLS-B8, etched in 3 H_2O : 1 HNO_3.

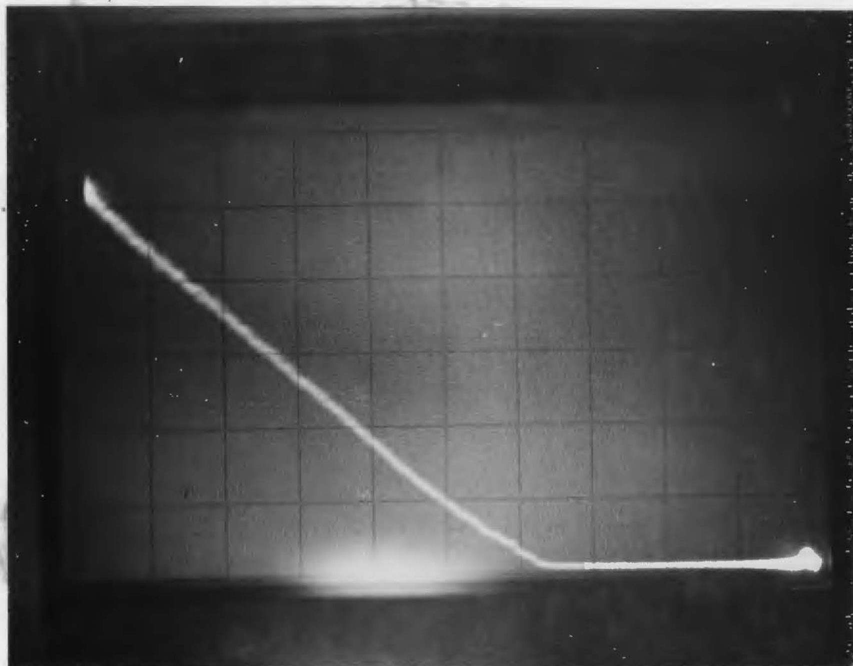

Fig. 9: Current vs Luminous power output, for ISM-B25.
Ordinate: 75 mW/div. Abcissa : 0.5 amp/div.

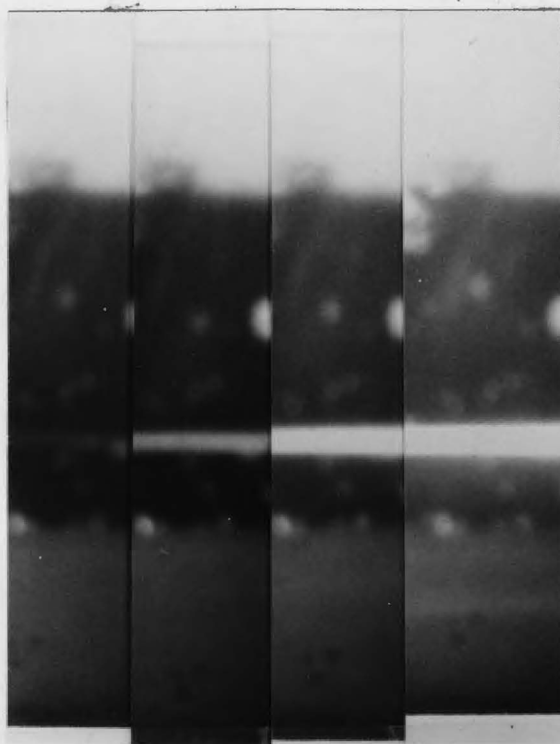

Fig. 10: Cleaved edge of ISM-B4, taken in infrared light, showing spread of scattered light primarily into thick first grown alloy layer. Applied current, from left : 6, 10, 20, and 40 mA.

Spectroanalysis of ISM runs

Fig. 11

WAFER NO.	PEAK WAVELENGTHS (±50 Å)	EMISSION ENERGY (eV)	CURRENT (mA)
ISM-B2	9160	1.35	5.0 and 10.0
	9200	1.35	100
	9260	1.34	200
ISM-B3	9000	1.38	10.0
	8860	1.40	100
ISM-B4 (1)	{ 8300	1.49	5
	{ 8330	1.49	10
(2)	8300	1.49	10
(3)	9070	1.37	10
(4)	{ 9080	1.37	10
	{ 9140	1.36	10
ISM-B25	8530	1.46	5.0 and 15.0
	8530	1.46 }	100
	9080	1.37 }	
	8000	1.55 }	
	8095	1.53 }	
	8160	1.52 }	200
	8380	1.50 }	
	8590	1.44 }	
	9100	1.36 }	
	8530	1.46 }	150
	9100	1.37 }	
ISM-B26	8950	1.39	5.0
ISM-B27	8670	1.43 }	10
	(∿9100 Å "shoulder")	(∿1.36) }	

Fig. 12: Cleaved end of laser chip, showing crack as well as parting lines.

System Parameters and Image Characteristics in Neutron Radiography

by

T.G. Blake

PART B: MCMASTER (ON-CAMPUS) PROJECT*

A project report submitted in partial fulfillment of the requirements for the degree of Master of Engineering

Department of Engineering Physics
McMaster University
Hamilton, Ontario

1972

* One of two project reports. The other part is designated PART A: INDUSTRIAL PROJECT

TITLE (PART B): System Parameters and Image Characteristics in Neutron Radiography

AUTHOR: T.G. Blake

SUPERVISOR: Dr. A.A. Harms

NUMBER OF PAGES: 48

MASTER OF ENGINEERING (Engineering Physics)

MCMASTER UNIVERSITY
HAMILTON, ONTARIO

ABSTRACT

This document reports the results of a study of several parameters of a neutron radiographic system of the direct conversion type, and of their effects on certain image characteristics. These parameters are: thickness of the converter, backing material of the very thin converter layers, level of water in the beam tube, exposure time, and film type. The image characteristics are relative optical density, specific contrast, and unsharpness, the latter interpreted quantitatively through the edge-spread function. Theoretical treatments and empirical data are presented and compared. Emphasis is put on investigations of the performance of thin (≤2000 Å) layers of gadolinium converter, and on the experimental analysis of the edge-spread function.

ACKNOWLEDGEMENTS

I would like to thank Dr. A.A. Harms, my project supervisor, for his guidance, R. Anderson, for technical assistance, P.S.W. Chan and P.K.H. Wong for helpful discussions on neutron beam flux and film response and Mrs. Mogensen for typing the report.

TABLE OF CONTENTS

		PAGE
I.	Introduction	1
II.	Experimental Facilities	
II.1	Beam Port	3
II.2	Photographic Materials	4
II.3	Densitometers	5
III.	Converter Studies	
III.1	Varying the thickness of gadolinium	6
III.1.1	Theoretical considerations	6
III.1.2	Experimental Investigations	6
III.2	Effect of backing materials	7
III.3	Results	8
III.4	Conclusions of converter studies	11
IV.	Factors affecting specific contrast and edge-spread: neutron thermalization, film type, and exposure.	
IV.1	General procedures	11
IV.2	Specific contrast results	13
IV.3	Unsharpness results	15
IV.4	Conclusions of contrast and unsharpness studies	17
V.	Summary and Recommendations	18
Appendix A:	Dependence of optical density on converter.	20
Appendix B:	Evaluation of density measurements; specific contrast.	22
Appendix C:	The effect of the form of the photomultiplier aperture configuration on the form of the observed edge-spread function.	25
References		28

LIST OF TABLES

PAGE

1. Comparison of the performance of thin gadolinium layers as converters, when backed by glass and by aluminum foil. Minimum water level, type M film. 29
2. Optical densities in the labelled regions of the images diagrammed in fig. 8, for several film types (T,M,R, Ortho, and 4489) and tube water levels (16.5, 20.0, 23.5, and 27.0 cm). 30
3. Measured mid-point slopes of the observed edge-spread functions. . . 32

LIST OF FIGURES

PAGE

1. The direct conversion neutron radiographic process. 33
2. The vertical beam port at the McMaster Reactor (not to scale). . . 34
3. (a) Converter grid for work on effect of gadolinium thickness. . . 35
   (b) Converter grid for work on effect of backing material. . . . .
4. Optical density as a function of gadolinium converter thickness for the range 0.2 - 25.4 μ, with D (.005 μ) = 0. Type M film, minimum water level. 36
5. Optical density as a function of gadolinium converter thickness for the range 50 Å - 2000 Å, with D(50 Å) = 0. Type M film, minimum water level. 37
6. Optical density as a function of gadolinium converter thickness, for two exposure times. Type M film, minimum water level. 38
7. Optical density as a function of gadolinium converter thickness for the range .005 - 2.6 μ, with D (.005μ) = 0. Type M film, minimum water level. 39
8. Diagram of pattern of composite image. 40
9. Specific contrast as a function of exposure time for various levels of water in the beam tube. Type T film. 41
10. Specific contrast as a function of water level for three exposure times. Type T film. 42
11. Specific contrast as a function of water level. Type T film, 20 min. and 40 min., and type R, 40 min. 43
12. Specific contrast as a function of water level, for 40 minute exposures, on Contrast Process Ortho and Electron Microscopy No. 4489 films. . 44

PAGE

13. Recorded edge-spread functions, type R film, 16.5 cm and 23.5 cm water levels. (Latter is normalized to contrast of former). 45

14. Normalized slope of edge-spread function at mid-point as a function of water level, for film types R, M, and T, 40 min. exposure. 46

15. Normalized mid-point slope of edge-spread function, as a function of exposure, for type R film, 16.5 cm water level. 47

16. Optical density gradient of a knife-edge image as a function of microdensitometer beam-width. Exposure 40 min., Ortho film. (after (13)). 48

I Introduction

The idea of neutron radiography was conceived by H. Kallmann[1] and initially developed by Kallmann and Kuhn[2]. However, only comparatively recently has the technique come to be used extensively in industry.

Radiography with neutrons of thermal energies (0.01-0.3 eV) has attracted the most interest, because the attenuation coefficients of these neutrons make them particularly complementary to x-rays in the information they may gather. While the attenuation of x-rays increases with the atomic number of the material, the attenuation coefficients of thermal neutrons is not a monotonic function of atomic number[3]. Some very light elements have very high coefficients, while most heavy elements are relatively transparent to neutrons; different isotopes of the same element may have high neutronic contrast.

The purpose of this project was to study several parameters of a radiography system and to investigate their effects on the characteristics of the recorded image. The neutron radiographic process, as employed herein, may be described as follows (see fig. 1). A collimated beam of neutrons is emitted vertically from a reactor core; it is thermalized after passing through a column of water at the bottom of the beam tube. The neutron beam is modulated by an object, then passes through a photographic film to impinge on a converter material. Many of the neutrons interact with nuclei of this high-cross section material, producing secondary radiation (e.g. internal conversion electrons, for a gadolinium converter), which creates the latent image in the film emulsion. This is referred to as the direct conversion technique.

Intuitively, the optical density in the image would be a strong function of the thickness of the converter, especially for thin layers of converter material. In this paper are described both experimental and theoretical studies of this relationship. Another important characteristic of the image is the

specific contrast which is a directly measurable value related to the optical density[4]. Its dependence on certain properties of the system is also investigated herein.

Elsewhere [5] a mathematical analysis of the radiographic process has been carried out for an object consisting of an infinitely narrow slit in an otherwise neutronically opaque field. Even though simplifications were made, the resulting expression for the image of the slit, the so-called "resolution function", could only be dealt with numerically. It was found, however, that the resolution function was well approximated by the normalized Lorentzian function,

$$R_L(x) = \frac{1}{1 + C_L x^2} \quad , \qquad (1)$$

where x is the perpendicular distance from the plane containing the slit and the axis of the neutron beam, and C_L is a constant determined by the properties of the system.

An infinitely narrow slit is an unattainable idealization, of course, but a straight edge, considered as the superposition of parallel slits covering half the object plane, is amenable to experimental study. By integrating $R_L(x)$ we get the "edge-spread function"[6],

$$f(x,C_L) = 1/2 + \frac{1}{\pi} \tan^{-1} (x \sqrt{C_L}) \quad , \qquad (2)$$

which has been normalized to unity at $x \to \infty$.

Obviously, this function (the E.S.F.) is closely related to the unsharpness of the image, which may thus be characterized by C_L. One part of the present

work involved the evaluation of the unsharpness of an image in terms of a measurable quantity, and the effect on this quantity of changing some of the properties of the system.

It is expected that these results will be useful in a basic way to future investigations of the physical processes involved in neutron radiography.

II Experimental Facilities

II.1 Beam Port

The work reported herein was performed with the McMaster University Reactor operating at 5 MW or 1.5 MW. A beam of thermal neutrons was extracted by means of a closed metal tube inserted vertically in a fuel rod position near the edge of the core (fig. 2).

The beam tube was 530 cm long and its inner diameter was 7 cm. Taking the thermal neutron source to be the column of water in the tube, the collimator ratio (L/d) of the beam would be 71.6 - 75.6[7,8]. The intensity of the virtually parallel beam was regulated by varying the height of water in the tube. Water could be pumped back and forth between the tube and a hold-up tank. The height of water in the tube was deduced from a scale reading giving the level in the tank. For the work described in section III, a "Snoopy" meter was used to monitor the flux near the top of the tube, and a tap in the water line was closed when the meter indicated a radiation level such that the reactor building exhaust alarm would not quite be triggered. The Snoopy meter was held in a precise location, pointing horizontally and in contact with the side of the beam tube. Its reading was then commonly 45 - 55 mrem/hour when exposures were made (in practice, the limit was found to be 60 - 65 mrem/hour).

This resulted in considerably higher flux levels than did the following procedure used in section IV.

The scale was calibrated by two set points. The first was the tank level when the tube was empty; because of the radiation hazard, this had to be read while the reactor was shut down. The other set point was the reading on the scale when the water in the tube was high enough to complete a circuit between two leads, deflecting an ammeter needle. Since both the tank and tube were cylindrical, these two points defined the linear relationsip between scale reading and tube level. To take evaporation into account, the second set point was rechecked before a set of exposures was made. Health Physics regulations then determined the minimum water level in the tube to correspond to a scale reading 24.0 cm above that of the second set point: this minimum corresponding to 16.5 cm of water in the tube, severely restricted the maximum beam intensity to $\sim 5 \times 10^6$ neutrons/cm^2 sec.

The neutron flux increased rapidly as the tube level approached its allowed limit, so the reproducability of the level was important. A routine was established which resulted in scale readings accurate to $\pm .02$ cm.

At the top of the beam tube was installed a working surface made of 1/4" aluminum insert. This table had screw holes positioned so that rails could be fastened to it. The film cassette was then slid over the neutron beam along these rails.

II.2 Photographic Materials

The film cassette of section IV was a flat, light tight aluminum box, with a sheet of gadolinium 25 μ thick fastened inside one wall. The walls were

felt-lined, and held the film pressed firmly between them when the cassette was closed. A vacuum cassette was used for the studies reported in section III; when evacuated, its flexible stainless-steel lid was sucked inward to press against the film, holding it hard against the converter.

A total of five different films were used in the course of the work: Kodak Industrial x-ray types T, M, and R, Kodak Electron Microscopy No.4489, and Contrast Process Ortho. The x-ray films were developed in Kodak x-ray type D developer at 25°C for 5 min. with agitation, stopped for 30 sec., fixed for at least 4 min. in Kodak x-ray fixer, and washed for 30 min. in cold running water. The Ortho film was developed for 3-1/2 min. in D-11 at 21.0 C, stopped, fixed for 4 - 5 min. in Acufix, and washed. The 4489 film was developed in D-19 (diluted 1:2) for 4 min. at room temperature, rinsed in room temperature water, fixed in Acufix for 8 - 10 min., and washed in cold water.

II.3 Densitometers

After the films were developed, two instruments were used to make optical density measurements. A Sakura PDA-80 portable densitometer took readings of the densities of the different regions of interest in each image, while a Leitz Wetzlar MPV scanning microscope photometer produced edge-spread functions by feeding a signal through a Photovolt multiplier (model 520-M) to a strip-chart recorder.

The Sakura densitometer was modified as follows. Some of the image regions to be inspected were too small to cover the photomultiplier aperture, so a thin piece of metal was affixed to each leg; the piece on the leg containing the opening contained a hole .093" in diameter. Since the reference point on the scale of the

instrument was simply associated with some maximum brightness observed by the photomultiplier, this adjustment in aperture size was just a constant factor that left the relative density readings unbiased.

For reasons given in Appendix C, the aperture of the scanning microdensitometer was chosen to be 23 μ wide by about 340 μ long. The microscope objective was 10 power. The scan speed was 12.5 μ/sec., and the strip chart speed was 0.5 in/sec., for a spatial relationship of film image to strip chart recording of 28.9 μ/in. ± 1.6%. This factor was found by measuring the separation, as recorded on the strip chart, of two well-located points on a photographic image scanned by the microdensitometer.

III Converter Studies

III.1 Varying the thickness of gadolinium

III.1.1 Theoretical considerations

A theoretical analysis of the dependence of optical density on the thickness of the gadolinium converter is given in Appendix A. The general appearance of this relationship, in fig. 4, has the exponential, asymptotic behaviour that would be expected intuitively. Another theoretical prediction[5], also shown in Fig. 4, is similar.

III.1.2 Experimental investigations

The validity of these analyses were tested experimentally by making exposures of various durations on type M film. A grid of Gd strips of different thicknesses was used as a converter. Layers of gadolinium 50 Å, 125 Å, 310 Å, 800 Å, and 2000 Å were deposited on aluminum foil by vapour-phase epitaxy at Welwyn Canada

Ltd., London, Ontario. Gadolinium sheet 25.4 in. thick is available commercially; to get thicknesses between 2000 Å (0.2μ) and 25.4 μ, the 25.4 μ sheet was machined by rolling it between pieces of stainless-steel-plated stainless steel (ferrotype). There resulted thicknesses of 20.1μ, 13.3μ, 7.2 μ, 5.2 μ and 2.6 μ, and a layer 1.1 μ thick which could not be removed from the ferrotype. These thicknesses were determined by multiplying 25.4 μ by the ratio of the original to the final area of the rolled piece of material.

The strips were then taped onto a piece of aluminum foil in the pattern shown in fig. 3(a), which was designed to keep all the different areas of interest inside a circle of diameter 3/4", small enough to be within the relatively uniform central portion of the beam. In the arrangement, it was attempted to place similar thicknesses alternately near the centre and near the edge of the grid, in order to even out effects due to spatial nonuniformity of the beam, which might be present to a significant extent even within that central region. This procedure was modified by the short length of some of the Gd strips that were rolled.

III.2 Effect of backing materials

To determine whether the backing material of the thin gadolinium layers would make a significant difference in film density, a grid was constructed as shown in fig. 3(b). The layers deposited on glass were too wide to fit them all into the beam at once, so only the 310 Å, 800 Å, and 2000 Å layers were compared. The 50 Å and 125 Å layers were included for completeness in measuring again the variation in optical density with converter thickness, thus repeating for confirmation part of the work of III.1.

It had been observed that the parts of the film that were not in front of gadolinium during the exposure, turned out darker if they were directly over the aluminum foil on which the grid was mounted; darker, in fact, than those areas over very thin Gd layers. To check whether this effect was causing the strips of Al foil backed gadolinium to produce blackening in addition to that due to the gadolinium alone, the foil to which the strips were taped was cut away so that parts of the strips had behind them the aluminum foil and other parts did not. Thus, if there was a source of error here, it might show up as a step in density of the images of the strips, as the densitometer was scanned across the position directly over the edge of the mounting foil.

III.3 Results

The densities were measured by manually scanning the Leitz microdensitometer beam across the region under consideration. The meter of the photomultiplier, rather than the strip chart recorder, was used to make the readings.

The results in figs. 4 and 5 show the relationship between the thickness of the gadolinium converter and the optical density produced, the densities measured relative to that associated with the 50 Å layer. Accompanying the experimental data are the results of theoretical analyses presented in Appendix A and by Garside and Harms[5]; both were calculated relative to the density at the 50 Å layer position and normalized to the experimental density asymptote. The values of the parameters (attenuation coefficients, etc.) which define the theoretical curves were obtained from Ref. 6. For the first curve, representing equation (A6), the constants K_o and K were taken to be the asymptotic value of density = 1.30 and $\sum + \alpha = .34$ respectively. The other theoretical curve was calculated

by the computer code (SQUANK III) used in Refs. 5 and 6; to adapt it for use with the double-coated type M film, the parameters for emulsion thickness and electron attenuation coefficient were varied, but the resulting curve was insensitive to these adjustments.

The empirical curve is seen to follow the forms of the theoretical ones, particularly at very small and very large values of converter thickness, where all the curves are linear and asymptotic respectively. However, discrepancies are clearly evident.

Further evidence of the linearity of the relation between density and converter thickness at very small thicknesses is given in fig. 6, which contains data taken from measurements on three different images having exposure times of 4 and 10 minutes. (A curve corresponding to a 7 minute exposure was parallel to the 4 minute curve). Although saturation is apparent in the 10 minute exposure, this graph still reinforces effectively the interpretation of fig. 5. It may be noticed that the curves do not appear to go to the origin, but to some considerable density at zero thickness. This is because the densities were not measured relative to the density corresponding to the 50 Å layer, and the density of the actual reference point was possibly anomalously low; further discussion on this point is given below.

In Table 1 is presented the comparison between the optical densities for gadolinium layers backed by aluminum foil and those for layers backed by glass. Corresponding values are equal for the 4 and 7 minute exposures, and significant differences appear only for the 10 minute exposure.

When these images were made, the foil-backed converter layers were taped to a piece of aluminum foil; as was referred to previously, film directly over

this foil was noticeably darker in the image. However, there was no detectalbe density step in area of the film over gadolinium, as the microdensitometer beam was scanned across the location of the edge of the piece of foil on which the conveter strips were mounted. Therefore, the radiation from the foil, or the radiation that induces it, did not penetrate the foil-backed gadolinium strips or the 25.4 μ all gadolinium strip. There remains the question of whether there is similar darkening from the gadolinium layers' foil backing itself. According to the results listed in Table 1 the effect is marginal; the thin Gd layers apparently diminished it. Here we interject that the areas of the film with neither gadolinium nor Al foil directly underneath were over a rough aluminum plate, which apparently had much less ability to darken the film than did the Al foil.

A more sensitive demonstration of the effect of the aluminum foil backing is fig. 7. This graph shows the transi#tion region between the results shown in fig. 4, relating to very thin deposited converter layers, and those of fig. 5, relating to the much thicker machined layers. The straight line through the sub-micron points passes below the 1.1 μ point. It is suggested that this is due to the foil backing, according to the following reasoning. Both the primary radiation impinging on the foil and the secondary or reflected radiation leaving it is attenuated exponentially by the gadolinium, but since the effect is very small, it is approximately linear with Gd thickness. Therefore, the curve through the sub-micron points remains a straight line but its slope is decreased; the thinner the layer, the more is the film blackened by the foil backing. Support for this interpretation may be found in fig. 6, in which the curves do not go to zero; this is due at least in part to the increased density produced by the backing under the thinner layers.

III.4 Conclusions of Converter Studies

In this section the dependence of optical density on gadolinium converter thickness was seen to have the expected form; it was linear for very thin converters (50 - 2000 Å), and asymptotic for relatively thick converters (>20μ). The simple theory formulated in appendix A was actually closer to the empirical results than was the more sophisticated computer-aided approach, but this may be because the latter was designed for application to single-emulsion films. The use of double-coated film may introduce more complexity than was anticipated, due to electrons slowing down in the film base before they reach the emulsion on the far side from the converter; radiation-to-blackness conversion efficiency is energy-dependent.

The form of the relationship for thicknesses in the Angstrom range was of some interest; the linearity in this range was established and reaffirmed, to within experimental uncertainty.

The choice of material on which the gadolinium layers were deposited was found to have a slight but definite effect. The aluminum foil backing increased the resulting density over that observed from layers backed by glass. The experimental curve in fig. 5 was then moved away from the theoretically predicted lines. Some kind of reflection or activation from the foil backing, as was observed from Al foil elsewhere in the images, was not entirely obscured by the thinnest gadolinium layers.

IV. Factors Affecting Specific Contrast and Edge-Spread: Neutron thermalization, film type, and exposure.

IV.1 General Procedures

The effects of three system properties on the unsharpness and specific

contrast of the image were investigated. These properties were: the height of water in the beam tube (upon which depends the intensity of the beam, and the thermalization of the neutron spectrum as well), the exposure time, and the type of film. The procedure was designed to reduce, in some respects eliminate, perturbations introduced by variables of development.

The films of each type were developed together, so that the temperatures of the chemicals were the same, and the process times could be made very similar for the films in each batch. For further uniformity, all six exposure times were represented on single pieces of film by sliding a cadmium plate in steps across the beam in front of the object plane. The details of this technique are as follows.

A rectangular piece of cadmium sheet, 6" x 1-1/2" x 1/16" was taped to the bottom of the cassette, so that when the cassette was placed in the beam and located by the rails, one edge of the Cd plate (the "straight edge") lay along a diameter of the beam. A similar plate of cadmium could be slid on the table surface to a position under the cassette which was raised by the rails.

The second plate would then cover part of the straight edge with respect to the neutron beam. In practice, the second plate was put in position first, then when the exposure was to be made, the cassette, loaded with film and with the straight edge attached, was put in its position. At timed intervals, the plate was pushed further under the cassette, covering more and more of the edge in steps of an eighth inch. In this way, 1/8" sections of a cadmium straight edge were exposed to the neutron beam for time intervals of 5, 10, 15, 20, 30, and 40 minutes, and these sections were located in a strip 3/4" long, within a central region of the beam having quite uniform intensity. The resulting image

was a pattern of the form depicted in the diagram of fig. 8. The pattern was labelled as shown to systemize the density readings and edge-spread scans, which were carried out using the portable densitometer and scanning micro-densitometer respectively.

While 1/16" of cadmium eliminates about 97% of the thermal neutrons, there are also gamma rays and epi-thermal neutrons coming out of the tube, and x-rays from neutron capture in the cadmium as well, which are not attenuated as severely. On the other hand, cadmium is far from transparent to this radiation and the results obtained from the measurements of image parameters could have been distorted by its effect. However, it was possible to use the analysis in Appendix B to take into account the spurious effects of any non-thermal neutron radiation.

IV.2 Specific Contrast Results

All the density measurements are given in Table 2. From these data, the corresponding values of contrast were calculated, according to the derivation in Appendix B. These values, for reasons given in the appendix, were considered more meaningful than the density readings themselves, and thus were used in the graphs, figs. 9 - 12. (See also Ref. 4)

First, fig. 9 is a plot of contrast vs exposure time (that is, the time of exposure to thermal neutrons), for the fast type T film at four levels of water in the beam tube. While for x-ray film exposed to electrons the density vs exposure curve (not to be confused with the density vs log exposure "characteristic" curve) is linear at low exposures and then becomes sublinear as saturation is approached[7], this graph shows that contrast decreases to zero

differently as the exposure is reduced to levels at which the film is insensitive and the image fades into fog. On the other hand, at the longer exposure times, the curves for all water levels show a tendency toward saturation. Of course, the water in the beam tube attenuates the beam, so the less water there is in the tube, the greater the actual exposure for a given time interval. It is seen in the graph that there is an early and severe onset of saturation corresponding to greatly reduced contrast, for type T film at the minimum water level. In fact, the severity of this saturation is even greater than might be expected, but it must be remembered that the rate of change of flux, as the water level was lowered to near the minimum, became extremely high.

The next graph, fig. 10, shows the relationship between contrast and water level for three exposure times of 10, 20 and 40 minutes on type T film. The effect of saturation is evident in the curve of the 40 minute exposure, as is the increasing insensitivity of the film for higher beam attenuation at the 10 minute exposure. In between, the contrast varies linearly with water level at the 20 minute exposure, an effect that is also apparent in the 40 minute curve before saturation is approached. However, it must be recognized that as the tube is filled with water and the beam is attenuated further, the contrast can not remain linear to intersect the axis but must tend asymptotically to zero. In any case, the straight line appears at the transition between curves of the other two types; the curves for 15 and 30 minute exposures were less extreme versions of the 10 and 40 minute curves respectively.

The two graphs, figs. 11 and 12, relate contrast to water level for the other four films, M, R, Ortho, and 4489, at 40 minutes exposure, and type M at 20 minutes as well. These curves all show the superlinear response of contrast to diminishing water level. They also indicate that the faster the film the

greater the contrast at a given water level and exposure time; but that this seems due to the fact that over the beam intensities available, contrast increased with film density - excepting the case of saturation of the type T emulsion - and of course density depends on film speed.

By a selection of data from Table 2, we see that where density and water height were equal, contrast does not necessarily increase with film speed. At 20.0 cm of water, type M film at 40 minutes has a density of 1.99 while type T at 15 minutes has a density of 2.00; the corresponding contrasts are 0.77 and 0.42 respectively. At the 16.5 cm level, Ortho film at 20 minutes and type R at 15 minutes both have densities of 0.77, but the calculated contrast of Ortho is 0.20 and that of type R is 0.14. This is the expected behaviour. Unfortunately not enough of these coincidences in density occurred to make a systematic analysis possible, and for the same reason, a study of contrast vs thermalization at constant density could not be obtained; this information would certainly be desirable.

IV.3 Unsharpness Results

Unshapness, or the "spread" of the edge-spread function[4], was taken to be effectively characterized by a single quantity, the slope of the E.S.F. at $x = 0$, with the height of the function normalized to unity and the x variable (referring to distance from the edge) in microns. This slope, the maximum value of the optical density gradient, depends on the size of the photometer aperture in the scanning microdensitometer. An analysis of this effect is described in Appendix C; the choice of a suitable aperture size was based on this analysis.

The chosen value of aperture width in the x-direction was 23 μ, and the length was chosen to be 340 μ, large enough to integrate out much of the noise in the image. The aperture then had the appearance of a long slit, parallel to the straight edge image it was scanned across.

A table of measured slopes of E.S.F.'s for various films, water levels, and exposure times, is given in Table 3. Simple calcualtions outlined in the appendix could be used to translate these slopes into such quantities as "true" E.S.F. slope, or C_L, but the aperture width was chosen to make the observed slopes suitable for the present purpose. Due to image noise, the exact form of the recorded E.S.F. depended strongly on the precise location of the scan. Where only one scan across a given section of the straight edge a smooth and reasonably symmetric curve, the slope at x = 0 of this curve was taken to be the valid one, and the uncertainty was that of measuring the slope. Where there were obtained several different smooth curves or none, an average value was used, and the corresponding uncertainty was larger.

Illustratively, fig. 13 contains traces of edge-spread functions recorded from type R film at the 16.5 and 23.5 cm water levels. The lower-contrast function corresponding to 23.5 cm of water has been normalized to the recorded contrast of the other, which is actual size. The difference in the normalized mid-point slopes of these curves is shown in the figure, and the image noise is also apparent, especially in those parts of the curves corresponding to low optical density.

The entries in the table for the 40 minute exposures at the 20.0 cm water level show the dependence of the slope on the film type. As would be expected, the slower, finer grain films have significantly larger slopes, or less unsharpness, than do the faster, coarser films.

The graph in fig. 14 shows the effect of water level on unsharpness for x-ray film types R, M, and T. Straight lines drawn through each set of points have comparable slopes, and indicate that the lower the water level, the less is the slope of the E.S.F., that is, a more thermalized neutron beam produces a sharper image.

However, it must be recognized also that the slope increased with decreasing exposure time, as shown in fig. 15. Thus, the beam attenuation associated with higher water levels has a part in the fore-going result as it reduces the exposure intensity.

IV.4 Conclusions of Contrast and Unsharpness Studies

It has been shown that contrast increases with exposure time and with decreasing water level, and the midpoint slope of the E.S.F., representing image "sharpness", decreases with increasing exposure time and with decreasing water level. It was also found that slower, finer-grained films had steeper E.S.F.'s and less contrast. However, when images of similar density were compared, the slower films had higher contrast, as might be expected[9]. While the information obtained in this part of the project is useful as it stands, particularly from the point of view of operating the radiography system by changing the tube water level and selecting the film type and exposure times, it would be of interest to investigate the effect of thermalization alone by studying images of the same mean density but made with different amounts of water in the beam tube. It is to be recognized that this would involve considerable effort, compensating precisely for beam attenuation by adjusting exposure times on a trial-and-error basis, since density itself should be

dependent on thermalization.

V Summary and Recommendations

In this work several fundamental aspects of neutron radiography have been systematically investigated, and a number of significant results obtained.

The dependence of optical density on converter thickness was measured for much thinner layers of gadolinium than has been previously reported. Qualitative agreement was found between experiment and two similar theoretical predictions, but a definite discrepancy was observed. Further theoretical analysis may be warranted, but for most purposes, the theory available would be regarded as adequate. Making exposures of thin converters on single coated films - although they are slower - might serve to clarify further some of the theoretical ideas.

For thin layers of converter, the backing material was seen to have some effect on the amount of blackening. Noticeable blackening was observed where the film was in front of aluminum foil alone, and this phenomenon also increased the density apparently due to gadolinium layers of thickness less than 0.2 μ on aluminum foil backing. It is believed that for this reason, the slope of the line through the experimental points in fig. 5 was decreased.

The image of a cadmium straight edge was used to determine the dependence of specific contrast and unsharpness on the beam tube water level, exposure time, and film type. The results were generally as would be expected from basic knowledge of radiography. The next step is to assume exposure time-intensity reciprocity, which is known to hold for the direct conversion, gadolinium converter technique[10,11], and then isolate variables affecting unsharpness and contrast by making the exposure level of the film the same for

the different values of the system parameters. According to [12], single emulsion film has less response to γ-radiation than does double emulsion film; although it is slower, and the effect was not very striking in the present work, this suggestion should be considered in further investigations. Also, γ shielding might improve visible contrast and unsharpness.

Two calculations of particular interest were performed and appear in the appendices. The theory of the relation of optical density to converter thickness was somewhat closer to the experimental result than a previous, more elaborate treatment, but this may simply exhibit the impossibility of adapting the single emulsion analysis to a double-emulsion system without doing more than just changing values of parameters to weighted averages. The central idea of the effect of the size and shape of the photometer aperture of the scanning microdensitometer on the results obtained (9, and Appendix C) helped to systemize the experimental measurement of the edge-spread function.

APPENDIX A

Dependence of optical density on converter thickness

The situation is represented by the schematic diagram of fig. 1. Considering a perfectly collimated beam of thermal neutrons and semi-infinite converter and emulsions (the film being double coated), we have for the neutron-nucleus interaction density at x_i,

$$\begin{aligned} f(x_i) &= \Sigma\ \phi(x_i) \\ &= \Sigma\ \phi(x_c)\ e^{-\ \Sigma(x_c - x_i)}\ \text{cm}^{-3}\ \text{sec}^{-1} \end{aligned} \qquad \text{(A-1)}$$

where Σ is the total macroscopic cross-section and $\phi(x)$ is the neutron flux at x.

Therefore, the conversion radiation (electron) flux at x_f is

$$\phi_e(x_f) = \int_{x_i=0}^{x_c} \Sigma\ \phi(x_c)\ e^{-\Sigma(x_c - x_i)}\ K(x_i \rightarrow x_f)\ dx_i \qquad \text{(A-2)}$$

where the electron transport kernel is assumed to be

$$K(x_i \rightarrow x_f) = \begin{cases} C_o\ e^{-\ \alpha_1(x_c - x_i)\ -\ \alpha_3(x_f - x_c)}, & x_f < x_c + a \\ C_o\ e^{-\ \alpha_1(x_c - x_i)\ -\ \alpha_3(x_f - x_i)\ -\ (\alpha_b - \alpha_3)b}, & x_c + a + b \leqslant x_f \leqslant x_c + 2a + b \end{cases} \qquad \text{(A-3)}$$

where C_o is an arbitrary constant and α_1, α_3(cf.Ref.5), and α_b are the electron attenuation coefficients in the converter, the emulsion, and the film base respectively.

Now the optical density of the developed film will be

$$D = \int_{t'=0}^{t} \left(\int_{x_f=x_c}^{x_c+a} + \int_{x_f=x_c+a+b}^{x_x+2a+b} \right) \varepsilon\phi_e(x_f)\ dx_f dt' \qquad \text{(A-4)}$$

for an exposure time t, where ε represents the electron-to-blackness conversion efficiency, and a is the emulsion thickness.

Substituting for ϕ_e, we integrate to obtain

$$D = \frac{\varepsilon\, C_o\; \Sigma\, \phi(x_c)t}{\alpha_3(\Sigma + \alpha_1)}\; (1-e^{-\alpha_3 a})\; (1+e^{-\alpha_b b-\alpha_3 a})\; (1-e^{-x_c(\Sigma + \alpha_1)}) \qquad \text{(A-5)}$$

This equation is of the form

$$D = K_o(1-e^{-K_1 x_c}) \qquad \text{(A-6)}$$

where K_o is the asymptotic value of D and $K_1 = \Sigma + \alpha_1$.

It may be noted that as x_c gets very small,

$$D \simeq K_o K_1 x_c,$$

a linear relationship, and

$$\lim_{x_c \to \infty} D = K_o.$$

APPENDIX B

Evaluation of density measurements; specific contrast

In addition to radiation from the (n,β) gadolinium reaction, there were obviously several other emulsion-detectable radiations present during exposures. These include background fog, uniform over the whole film, and, in the beam, γ-rays and epithermal neutrons that interact with the gadolinium but not with the cadmium. There were also γ-rays emitted in the dominant radiative capture reaction of the cadmium. The effect of all of this radiation on the composite images studied in this investigation is, on the surface, complex, due to the fact that it is partly attenuated or even created at the cadmium plates. However, what is desired is a series of readings giving the contrast of 1/16" of cadmium for different exposure times, and it turns out that these numbers are easily calculated.

First, consider the observed density on the "open" side of the straight edge in terms of the components that contribute to it, in the notation of fig.B

$$D_i = Nt_i + D_\gamma t_i + (40-t_i)\, D_s, \qquad \text{(B-1)}$$

where t_i is the time of exposure to thermal neutrons, in minutes.

N_i is the film darkening per minute due to thermal neutron interacting with the converter (where there is no cadmium to impede the neutrons),

D_γ is the darkening per minute due to other radiation in the neutron beam,

D_s is the darkening per minute due to all the radiation in the beam attenuated by 1/16" of cadmium, plus the capture radiation from the cadmium;

and the total time the film is exposed to the beam is 40 minutes.

On the cadmium side of the straight edge, the observed density is

$$D_i' = D_s t_i + (40-t_i)\, D_{ss}, \tag{B-2}$$

where D_{ss} is the darkening per minute due to the beam radiation when impeded by two 1/16" plates of cadmium, and is obtained by doubling the value of the cadmium thickness wherever it appears in the expression for D_s.

Now, if the cassette had been removed from the beam after time t_i, the observed densities (the "true", or intended, densities) would have been

$$D_{ti} = D_i - (40-t_i)\, D_s, \tag{B-3}$$

and

$$D_{ti}' = D_i' - (40-t_i)\, D_{ss} \tag{B-4}$$

and the observed contrast would have been

$$\Delta D_{ti} = D_{ti} - D_{ti}' = D_i - (40-t_i)\, D_s - t_i D_s = D_i - 40\, D_s \tag{B-5}$$

But when $t_i = 40$ (i=6, fig.8), we have

$$D_i' = D_6' = 40\, D_s$$

Therefore, the true contrast to be quoted is just

$$\Delta D_{ti} = D_i - D_6' \tag{B-6}$$

Intuitively, this result would be expected, because after time t_i, $D_i' = D_6'$, and the region of D_i is then convered by the single layer of cadmium for a time $40 - t_i$, as is the region of D_6' (which is always covered by that amount of cadmium). Thus, the same density should be added to both D_i and D_6' in the time $40 - t_i$. (Note: D_o should serve as well as D_6', but despite contraintentions,

the region of D_0 experienced a spatial gradient in beam intensity. See Table 2.) The region of D_i', on the other hand, is then covered by two attenuating sheets of cadmium, and the density added there is not the same as in D_i or D_6'. It is less, which is why the calculated contrasts for some of the lightly exposed areas of the films (and see fig. 10) are practically zero, while there is a definite arithmetic difference between D_i and D_i', and in fact contrast is visible to the eye; the contrast is due to the non-thermal neutron radiation impinging on the system after the area in question is covered by the cadmium plate.

APPENDIX C

The effect of the photomultiplier aperture configuration on the form of the observed edge-spread function

In the edge-spread scanning part of the experiment, special attention was given to the effect of the shape and size of the area on the film sampled by the microdensitometer. This appendix reproduces the treatment of this problem appearing in Ref. 13.

Calculations are made much simpler if the opening is rectangular. The length should be large, to integrate out the noise of the image, but the width is a trade-off between integrating the noise out of the recorded function and accurately measuring the density variation at each point across the edge. Also, it was clear that the Lorentzian approximation to the edge-spread function would have to be used for the analysis.

The E.S.F. is then given by

$$f(x,C_L) = \frac{1}{2} + \frac{1}{\pi} \tan^{-1} (x\sqrt{C_L}) \ . \qquad \text{(C-1)}$$

The function observed by the scanning microdensitometer and recorded on the strip chart is

$$g(x,C_L) = \frac{1}{\Delta} \int_{x-\Delta/2}^{x+\Delta/2} f(x',C_L)\, dx', \qquad \text{(C-2)}$$

where Δ is the width of the photomultiplier opening.

Now the shape of the E.S.F., $f(x,C_L)$, is characterized by the number C_L, which also characterizes $g(x,C_L)$. If C_L can be calculated from an analysis of the recorded $g(x,C_L)$, this value of C_L then defines the true resolution, or more precisely, the unsharpness (7), of the neutron radiographic system. A con-

venient parameter of $g(x,C_L)$ which contains the required information is the normalized slope at $x = 0$.

$$S_{go} = \frac{\delta g}{\delta x}\bigg|_{x=0} = \frac{2}{\pi\Delta} \tan^{-1} \frac{\Delta\sqrt{C_L}}{2}. \qquad \text{(C-3)}$$

The slope at $x = 0$ of the "true" E.S.F. is

$$S_{fo} = \frac{\delta f}{\delta x}\bigg|_{x=0} = \frac{\sqrt{C_L}}{\pi},$$

$$S_{go} = \frac{2}{\pi\Delta} \tan^{-1} (\pi \Delta S_{fo}/2), \qquad \text{(C-5)}$$

Note that $\lim_{\Delta \to 0} S_{go} = S_{fo}$,
and $\lim_{\Delta \to \infty} S_{go} = 0$.

As Δ, the aperture width, gets large, S_{go} bears less and less relation to S_{fo}, until ultimately, most of the step in density near $x = 0$ is contained in the opening at once, and $S_{go} \to \frac{1}{\Delta}$.

We may describe the E.S.F. by S_{fo}, which by (C-4) is equivalent to describing it by C_L. Measuring S_{go} we can use (C-5) to get S_{fo}, more reliably if Δ is small compared to the distance over which the edge spreads. However, as Δ gets smaller, noise in the image tends to obscure the shape of the observed $g(x,C_L)$.

To find the optimum width, edge-spread functions were recorded with different aperture widths, at the same place in an image on Ortho film of a cadmium knife-edge 1/16" thick with 16.5 cm of water in the beam tube. Due to an inability to exactly reposition the film before each scan, there was some lack of reproducability, but as fig. 16 shows, the measurements agree quite well with the above theory. From the graph, and the appearance of the recorded E.S.F.'s, it is apparent that an opening 23 μ wide would be optimum for Ortho

film; since the fine-grain Ortho was among the highest resolution of the films, and the same opening had to be used for all scans for direct comparisons to be meaningful, the 23 μ width was chosen. In practice, a convenient setting for the opening length was found to be 340 μ.

REFERENCES

1. H. Kallmann, Research, 1, p.254 (1948)

2. H. Kallmann and E. Kuhn, U.S. Pat. #2, 186,757 (1937)

3. R. Matfield, Atom, #174, p.84 (Apr. 1971)

4. I. Panaitescu, Mat. Eval., July 1971, p.153

5. B.K. Garside and A.A. Harms, J. Appl. Phys. 42, #12, p.5161-67 (Nov. 1971)

6. A.A. Harms, B.K. Garside and P.S.W. Chan, J. Appl. Phys., 43, #9, 3863-67 (Sept. 1972)

7. T. Inouye and K. Ogawa, Nucl. Instr. and Math., 42, p.309-11 (1966)

8. W.L. Whittemore, Gulf General Atomic Report, GA-9472, July 7, 1969

9. M. deBalder, 6th ICNT, Vol. D, p.127 (1970)

10. R.C. Valentine,"Response of Photographic Emulsions to Electrons", Advances in Optical and Electron Microscopy, Academic, New York, Vol. 1, 1966

11. M.R. Hawkesworth, J. Sci. Instr., Series 2, Vol. 2, p.673 (1969)

12. H. Berger, Mat. Eval., p.55(March, 1972)

13. A.A. Harms and T.G. Blake, Trans. Am. Nucl. Soc., 15, p.710 (Nov. 1972)

GENERAL REFERENCES

14. R.H. Herz, "Photographic Action of Ionizing Radiations", Wiley-Interscience, 1969

15. H. Berger, "Neutron Radiography", Elsewier, New York, 1965

Table 1: Comparison of the performance of thin gadolinium layers as converters when backed by a glass and by aluminum foil. Minimum water level, type M film.

Exposure Time (mins.)	Thickness	2000 Å	800 Å	310 Å
4	Density for glass backing	0.85 ± .005	.035 ± .005	.017 ± .003
	Density for foil backing	0.90 ± .005	.037 ± .004	.019 ± .004
7	Density for glass backing	.165 ± .005	.105 ± .010	.077 ± .007
	Density for foil backing	.165 ± .010	.103 ± .005	.079 ± .004
10	Density for glass backing	.240 ± .010	.098 ± .004	.052 ± .003
	Density for foil backing	.255 ± .005	.115 ± .006	.065 ± .005

Table 2: Optical densities in the labelled regions of the images of fig. 8, for several film types and tube water levels (Uncertainties in D_i are ±2%, but with max. .02, min. .01 div.).

Type T	D_R	D_o/D_o'	D_1/D_1'	D_2/D_2'	D_3/D_3'	D_4/D_4'	D_5/D_5'	D_6/D_6'
16.5	.16	2.22 / 1.88	2.61 / 1.97	1.94 / 2.06	3.18 / 2.17	3.30 / 2.32	3.37 / 2.43	3.40 / 2.52
20.0	.17	1.37 / 1.19	1.61 / 1.25	1.81 / 1.30	2.00 / 1.37	2.17 / 1.43	2.47 / 1.51	2.71 / 1.58
23.5	.17	1.04 / .93	1.19 / .98	1.32 / 1.01	1.43 / 1.06	1.57 / 1.10	1.77 / 1.13	1.95 / 1.18
27.0	.18	.78 / .71	.88 / .74	.94 / .77	1.01 / .79	1.08 / .82	1.20 / .86	1.31 / .89
Type M								
16.5	.30	1.59 / 1.38	1.87 / 1.46	2.08 / 1.51	2.28 / 1.57	2.48 / 1.62	2.83 / 1.71	3.07 / 1.78
20.0	.30	1.09 / .99	1.23 / 1.03	1.34 / 1.06	1.47 / 1.09	1.58 / 1.12	1.77 / 1.17	1.99 / 1.22
23.5	.30	.88 / .81	.96 / .83	1.02 / .87	1.08 / .88	1.14 / .90	1.27 / .93	1.38 / .96
27.0	.30	.70 / .66	.72 / .67	.77 / .68	.79 / .69	.80 / .70	.84 / .71	.88 / .72

Table 2, continued

Type R	D_R	D_o/D_o'	D_1/D_1'	D_2/D_2'	D_3/D_3'	D_4/D_4'	D_5/D_5'	D_6/D_6'
16.5	.17	.57 / .48	.64 / .50	.70 / .52	.77 / .54	.83 / .57	.94 / .60	1.07 / .63
20.0	.17	.35 / .31	.40 / .33	.44 / .34	.49 / .36	.52 / .37	.60 / .38	.64 / .39
23.5	.16	.29 / .27	.30 / .27	.32 / .28	.34 / .28	.37 / .29	.40 / .30	.43 / .30
27.0	.16	.23 / .21	.24 / .21	.25 / .22	.26 / .22	.27 / .23	.29 / .23	.30 / .23
Ortho								
16.5	.07	.47 / .40	.57 / .42	.63 / .44	.69 / .46	.74 / .48	.85 / .51	.96 / .54
20.0	.07	.20 / .17	.23 / .18	.26 / .19	.29 / .20	.30 / .21	.34 / .22	.39 / .23
23.5	.07	.17 / .16	.18 / .16	.20 / .16	.21 / .16	.22 / .17	.24 / .17	.28 / .18
27.0	.07	.17 / .16	.19 / .16	.20 / .17	.20 / .17	.23 / .17	.24 / .18	.27 / .19
4489								
16.5	.07	.14 / .13	.17 / .14	.19 / .14	.21 / .14	.24 / .16	.28 / .17	.32 / .17
20.0	.07	.12 / .11	.13 / .12	.14 / .12	.16 / .12	.18 / .12	.20 / .13	.21 / .13
23.5	.07	.10 / .10	.11 / .10	.12 / .10	.12 / .10	.13 / .10	.14 / .10	.15 / .10
27.0	.06	.09 / .09	.10 / .09	.10 / .09	.10 / .09	.10 / .09	.11 / .10	.12 / .10

Table 3: Measured mid-point slopes of the observed edge-spread function.

Film Type	Exposure Time (mins.)	Tube Water Level	Normalized slope of edge-spread function at x = 0 (x $10^{-2}\mu^{-1}$) (Underlined values plotted. See text)	Uncertainty in plotted value (x $10^{-2}\mu^{-1}$)
R	40	16.5	1.88, 1.74	±.1
	30	16.5	2.00, 2.03	±.05
	20	16.5	2.32, 2.22, 1.93; Avg. 2.13	±.2
	15	16.5	2.22	±.05
	10	16.5	2.95, 3.20, 2.46, 2.84; Avg. 2.65	±.2
	5	16.5	2.84, 2.70; Avg. 2.77	±.07
	40	20.0	1.67, 1.99; Avg. 1.82	±.15
	40	23.5	2.16	±.1
	40	27.0	2.26, 2.62, 3.01	±.1
T	40	20.0	1.56, 1.49	±.05
	40	23.5	1.69, 1.63; Avg. 1.66	±.05
	40	27.0	1.92	±.05
M	40	20.0	1.58, 1.55	±.05
	40	23.5	2.25, 1.76, 1.94; Avg. 1.98	±.25
	40	27.0	1.88, 2.34, 2.07	±.2
Ortho	40	20.0	2.02, 1.84, 2.00	±.05
4489	40	20.0	2.49, 3.26, 2.60; Avg. 2.87	±.4

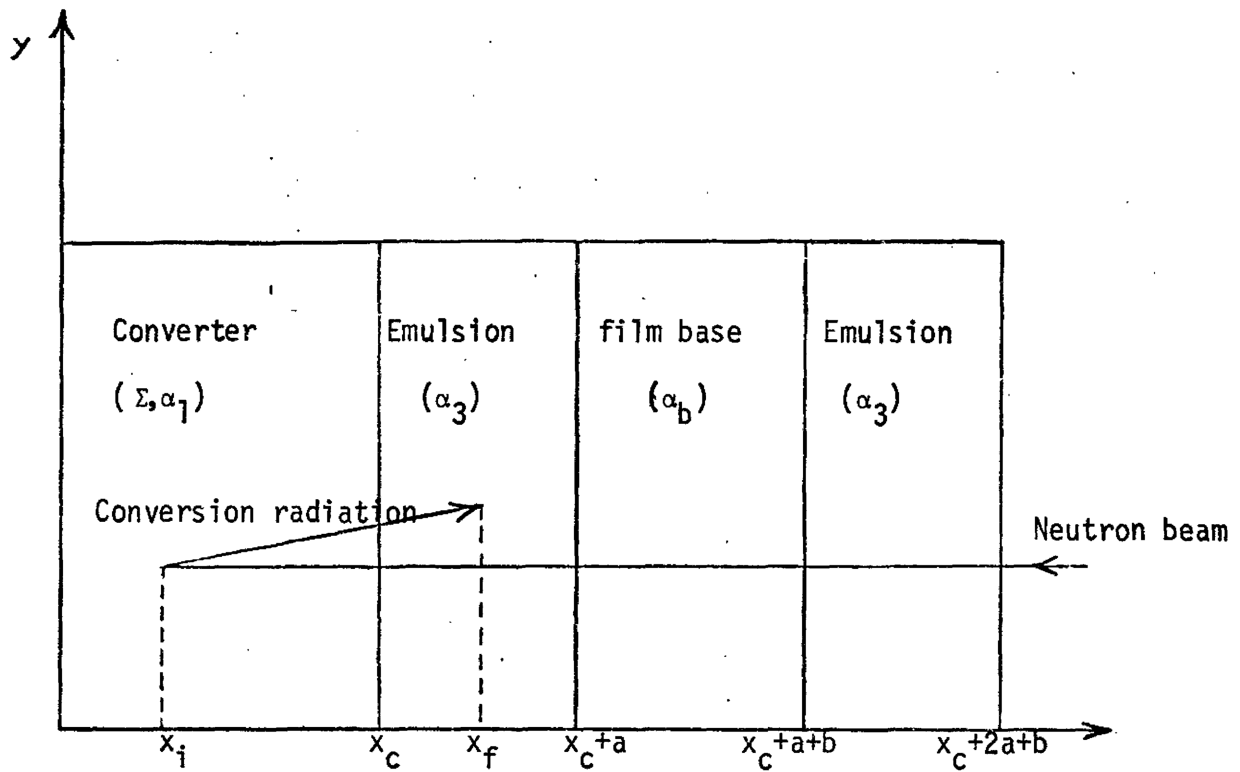

Fig. 1: The direct conversion neutron radiographic process

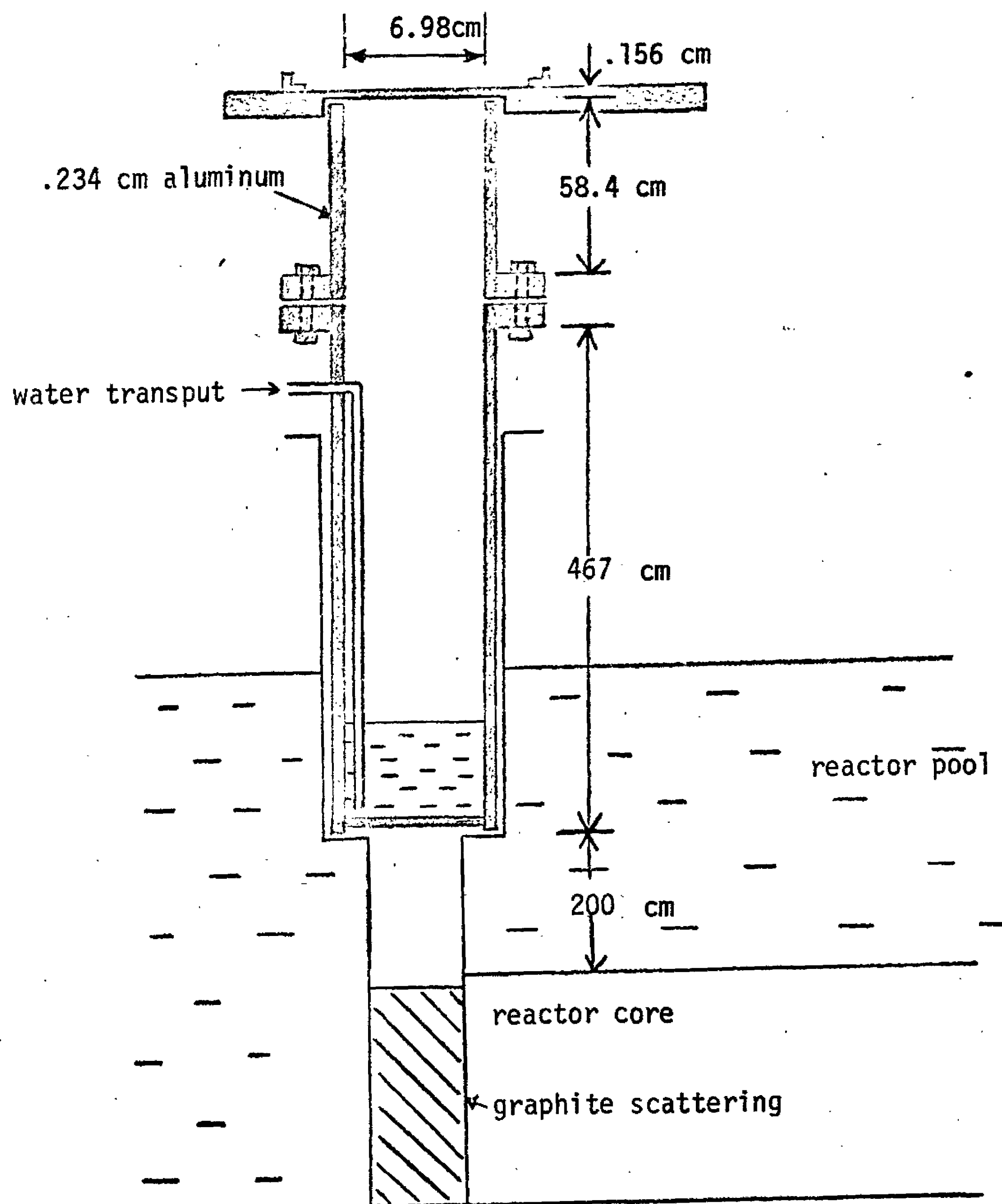

Fig. 2: The vertical beam port at the McMaster University Reactor (not to scale).

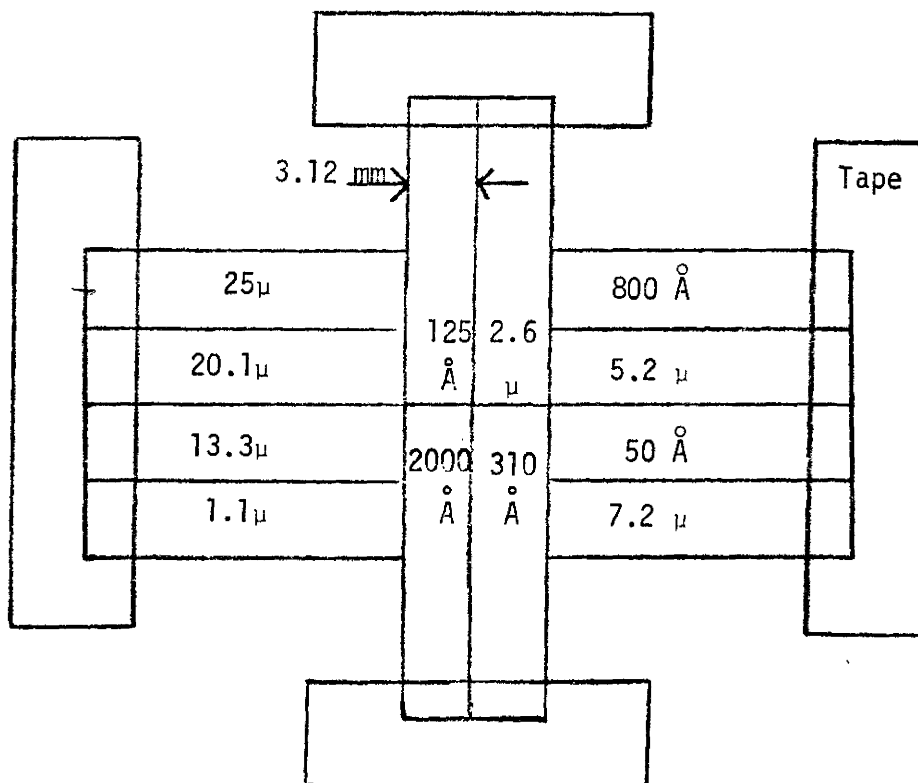

Fig. 3(a): Converter grid for work on effect of gadolinium thickness

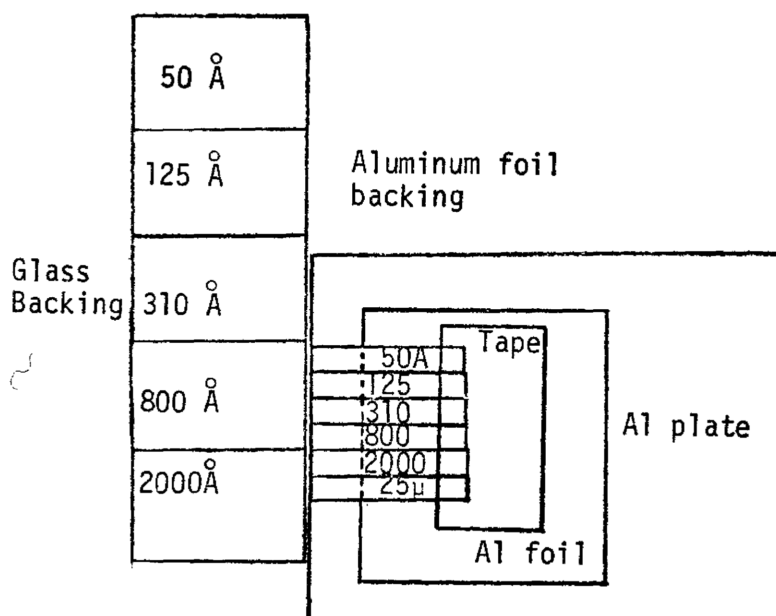

Fig. 3(b): Converter grid for work on effect of backing material

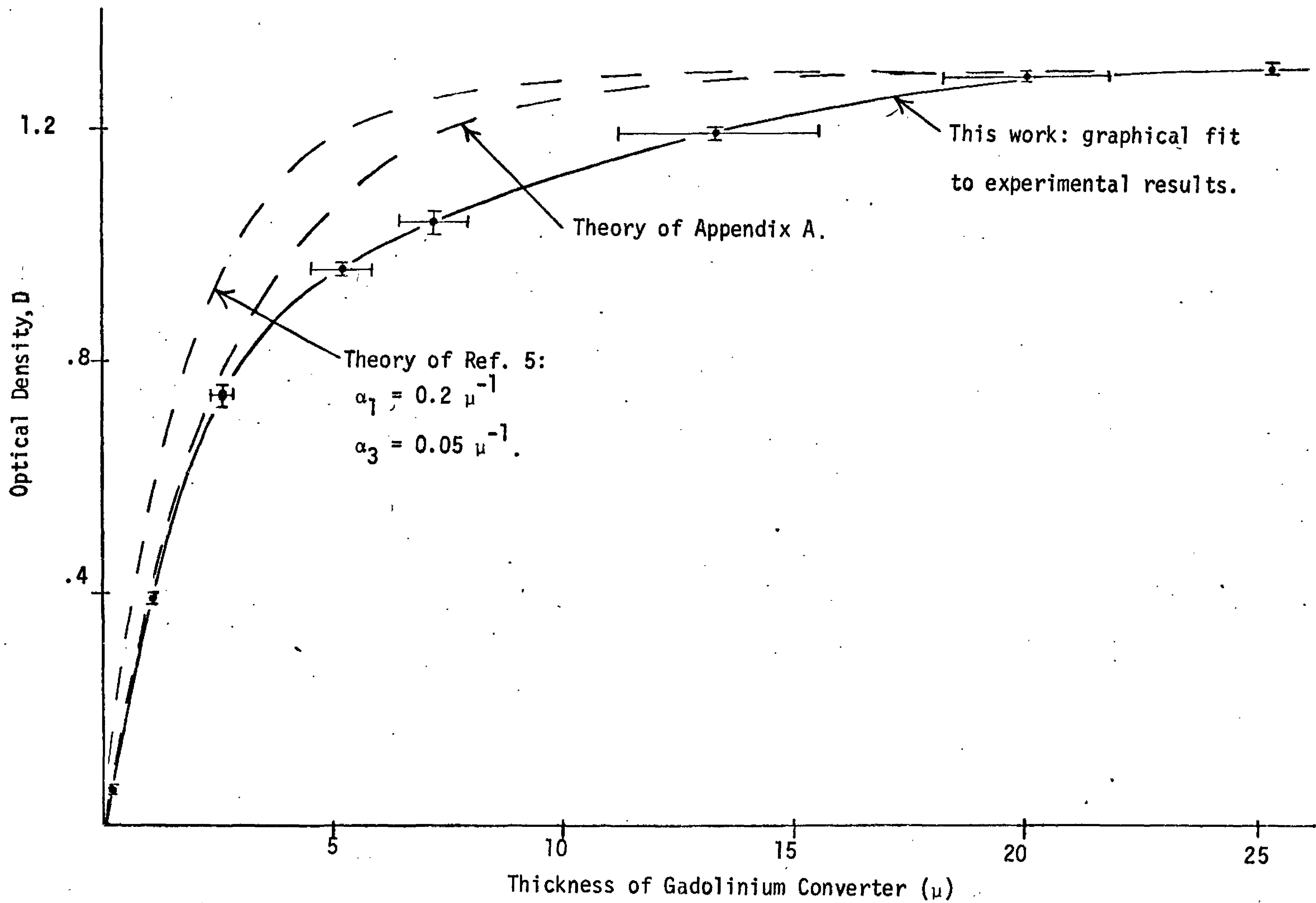

Fig. 4: Optical density as a function of gadolinium converter thickness. D is density referred to $D(.005\mu) = 0$. Type M Film, minimum water level.

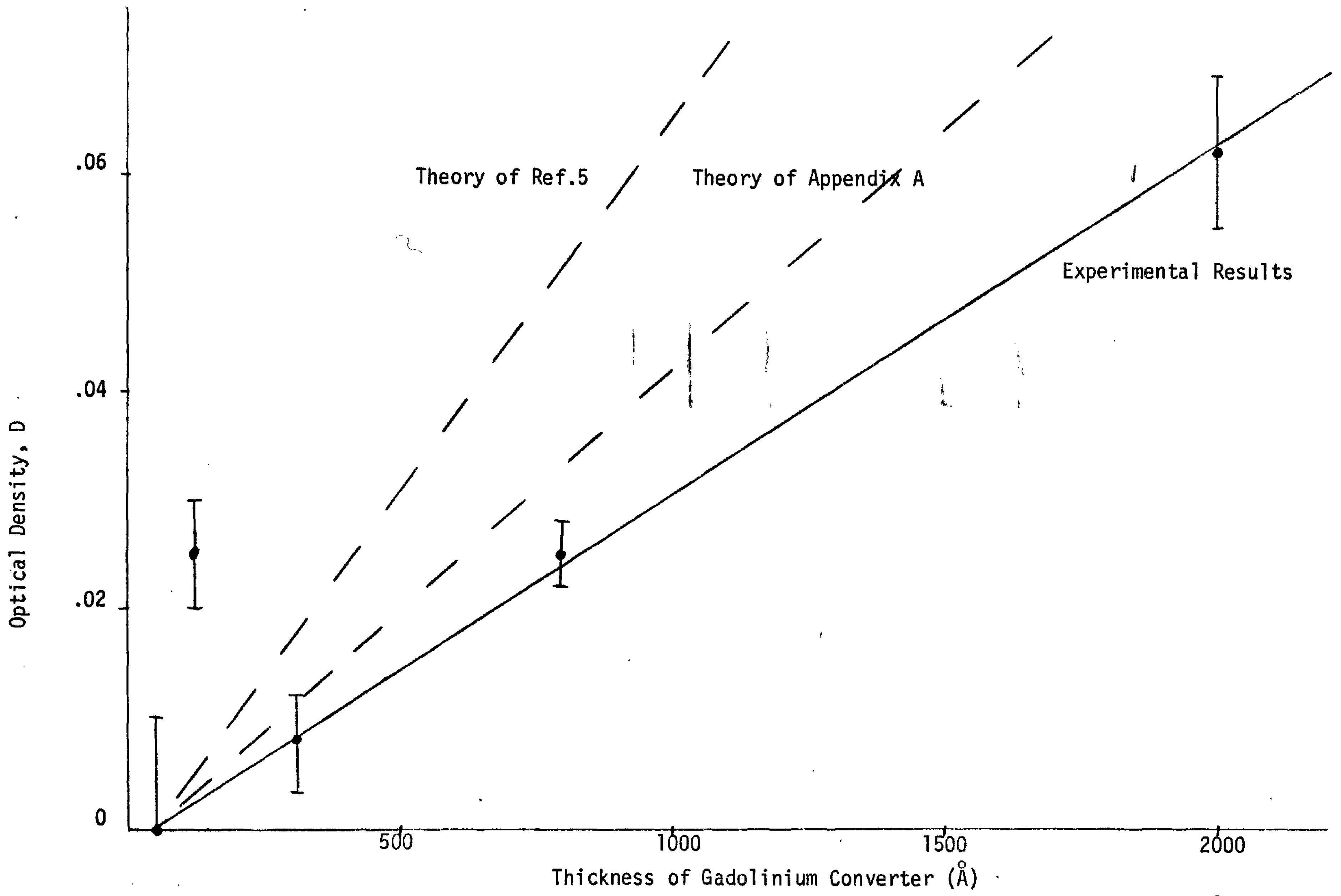

Fig. 5: Optical density as a function of gadolinium converter thickness. D is referred to D(50Å)= 0. Type M film, minimum water level.

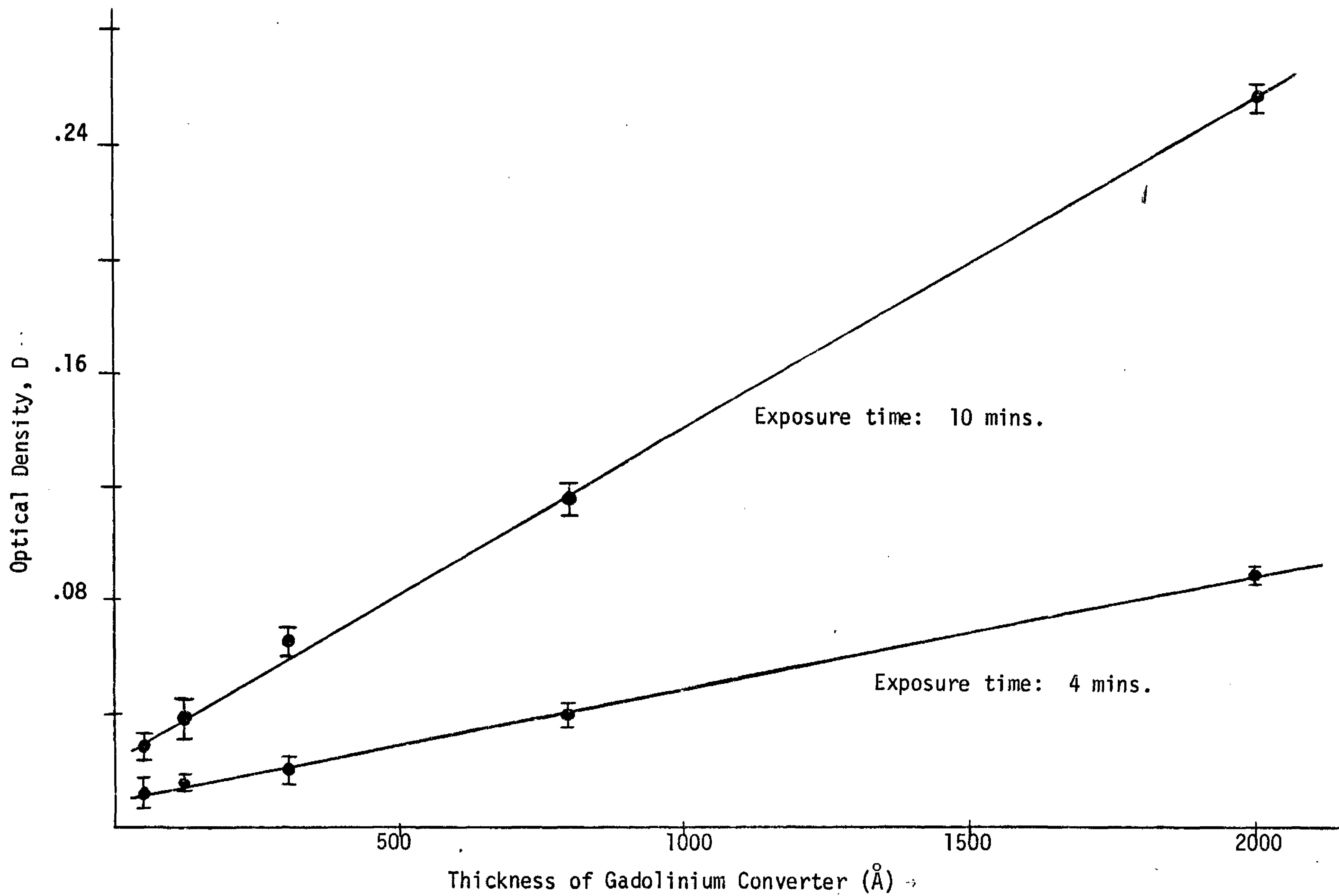

Fig. 6: Optical density as a function of gadolinium converter thickness, for two expsoure times. Type M film, minimum water level.

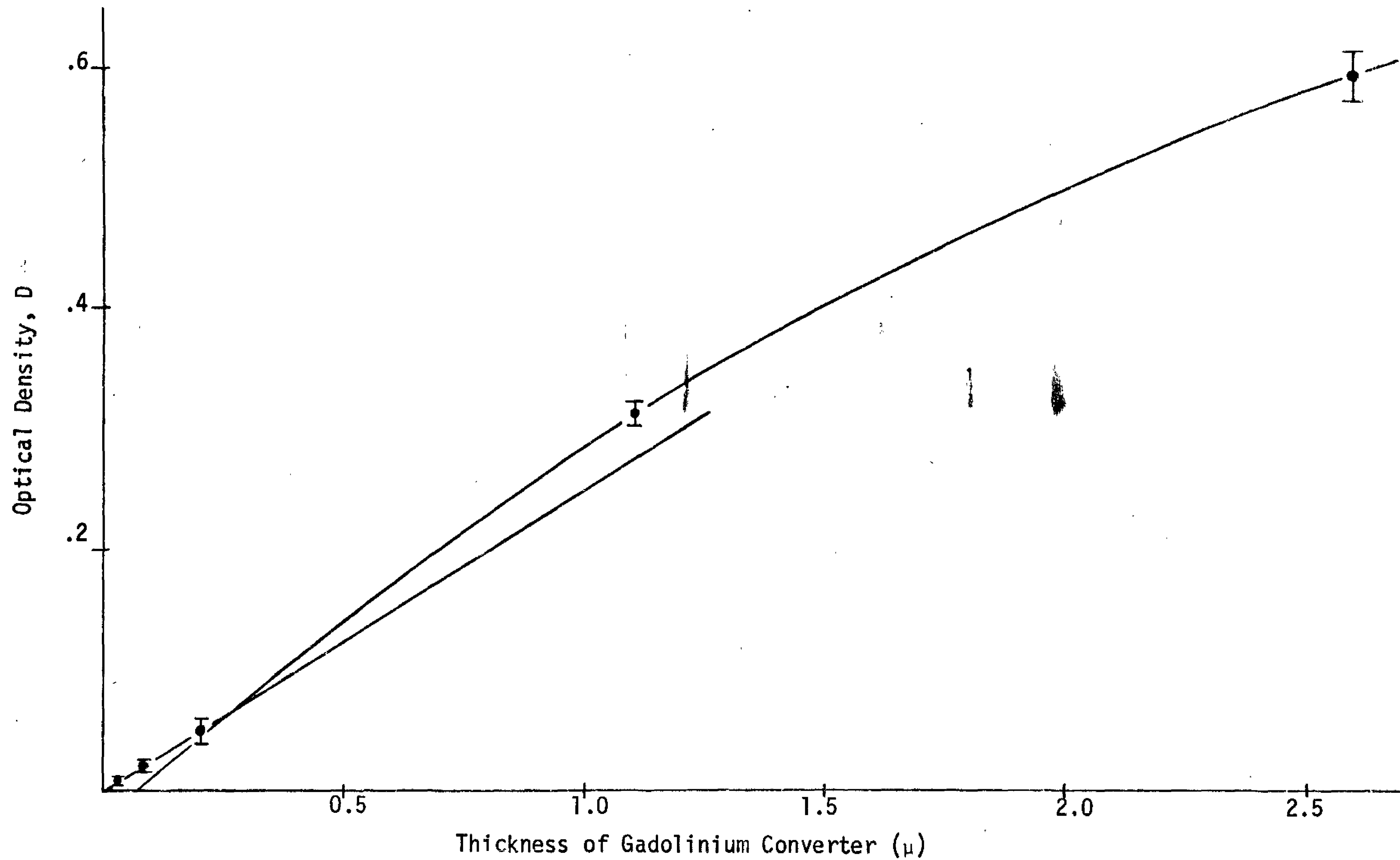

Fig. 7: Optical density as a function of gadolinium converter thickness, with D(.005μ)= 0. Type M film, minimum water level.

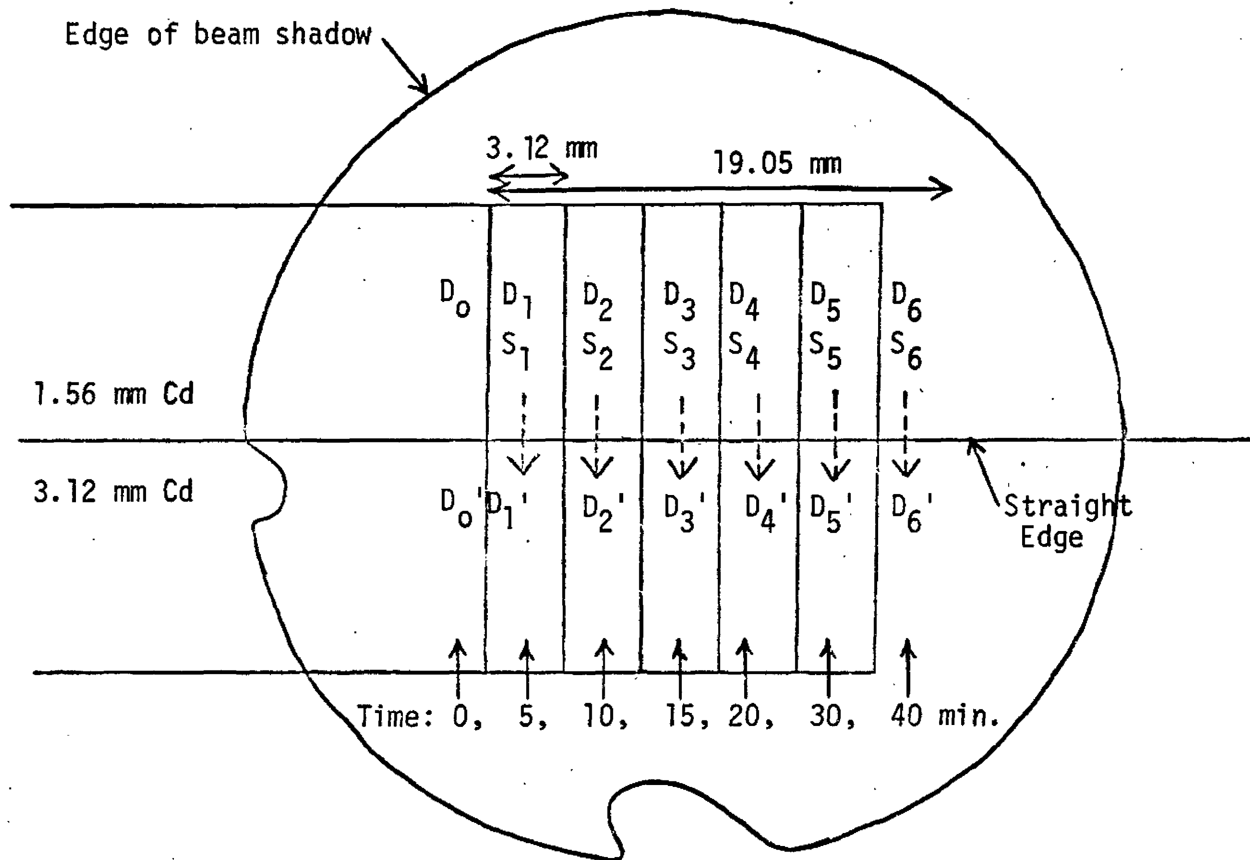

Fig. 8: Diagram of pattern of composite image.

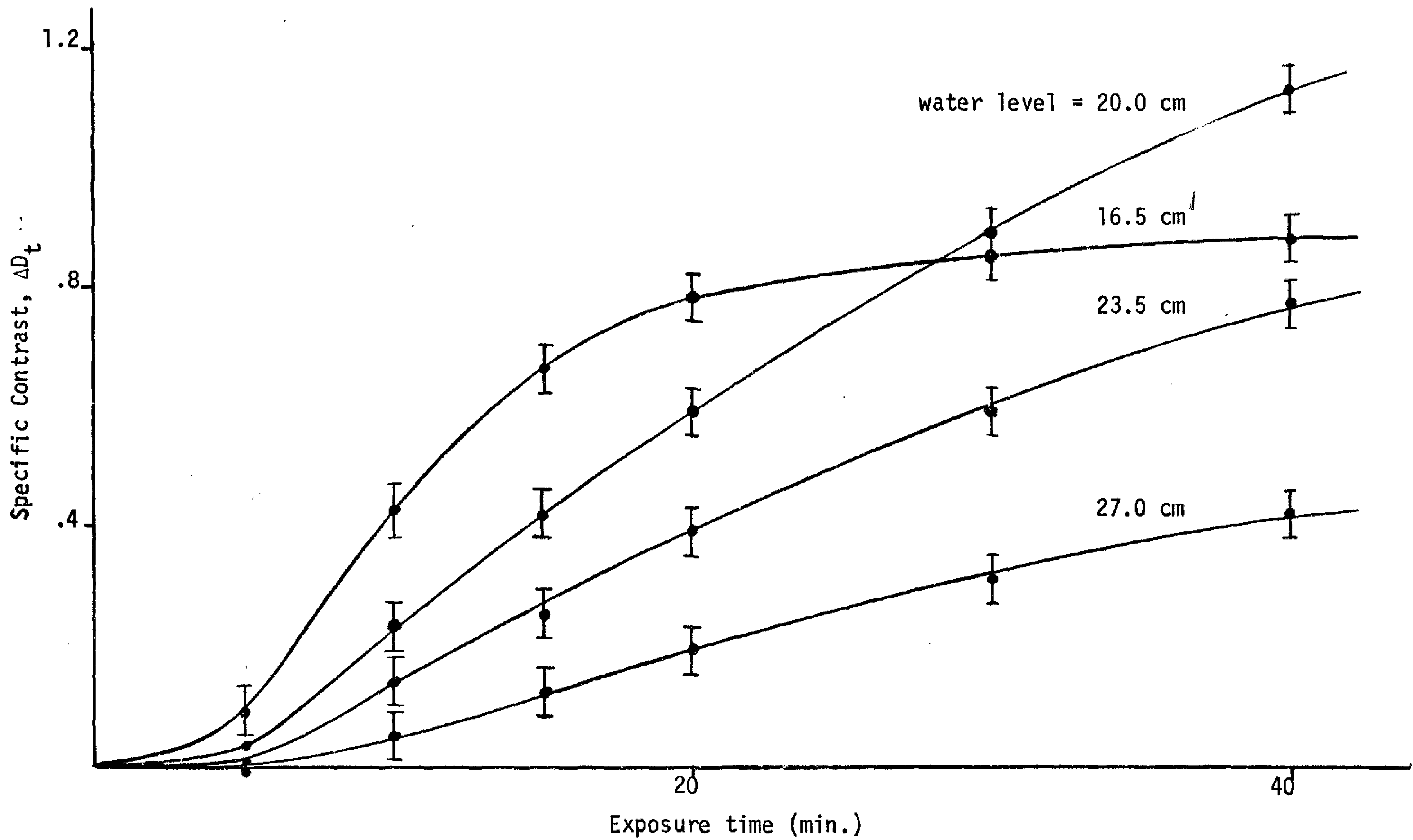

Fig. 9: Specific contrast as a function of exposure time for various levels of water in the beam tube. Type T film.

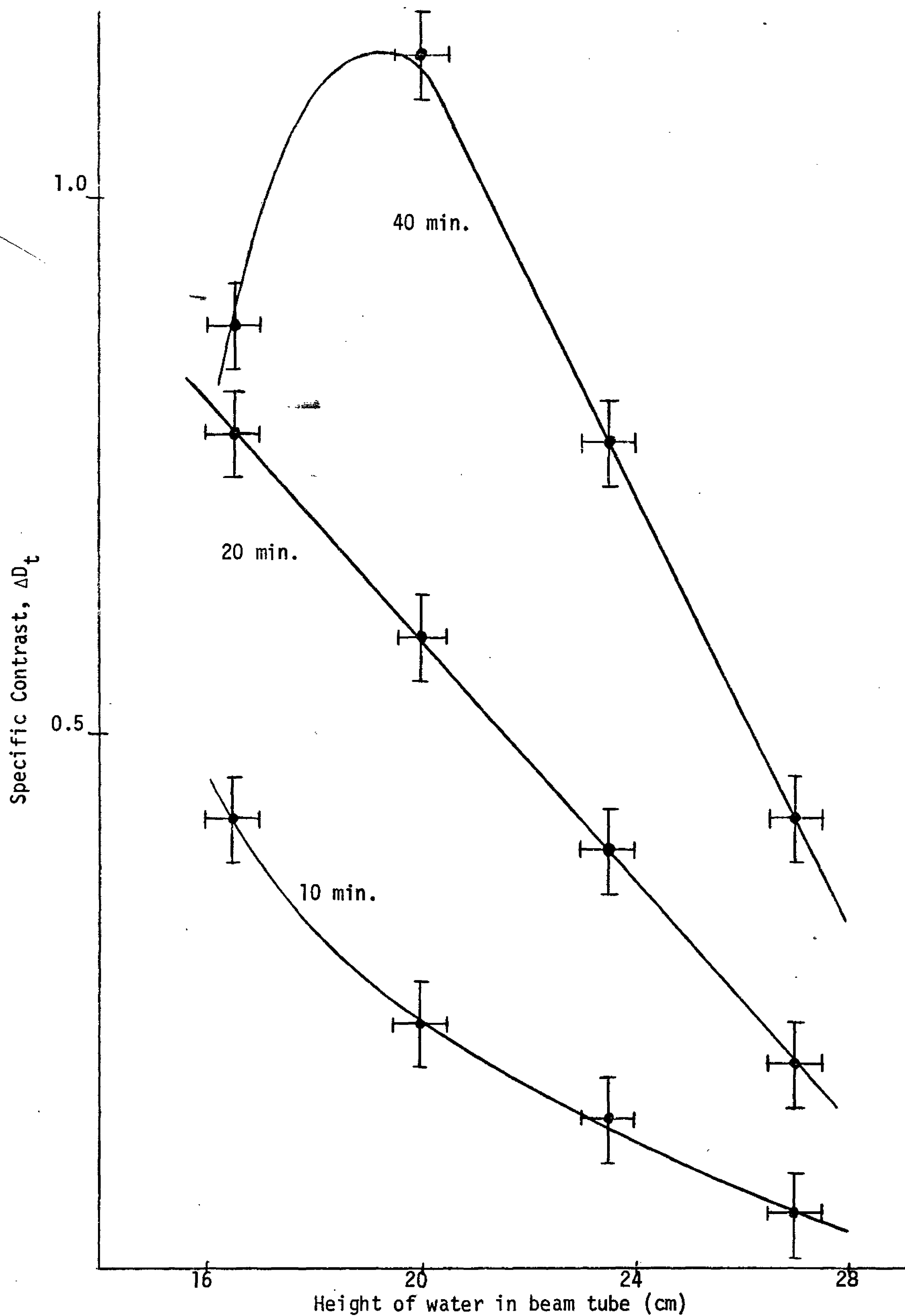

Fig. 10: Specific contrast as a function of water level for three exposure times on type T film.

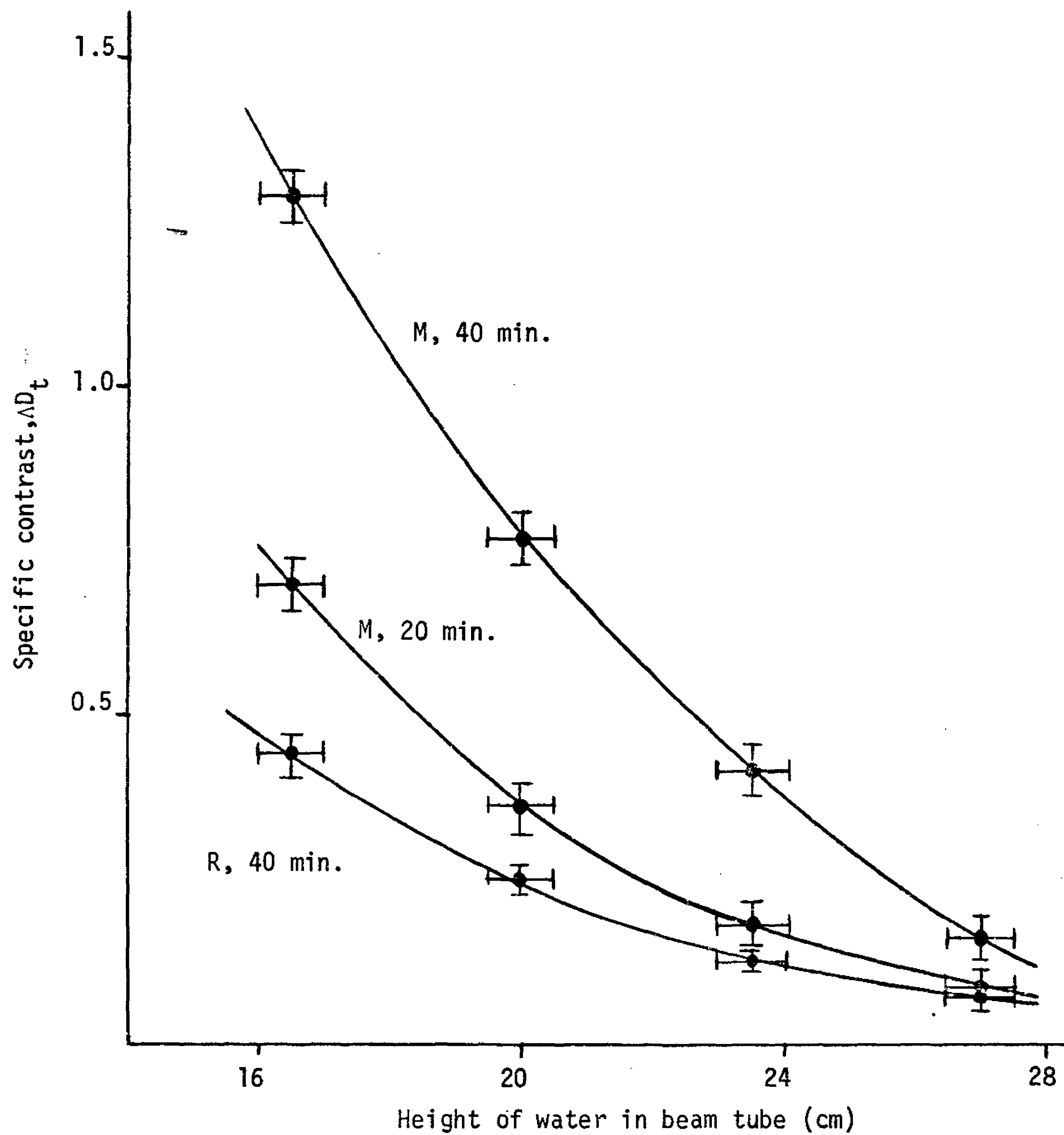

Fig. 11: Specfic contrast as a function of water level. Type M film, 20 min. and 40 min., and type R, 40 min.

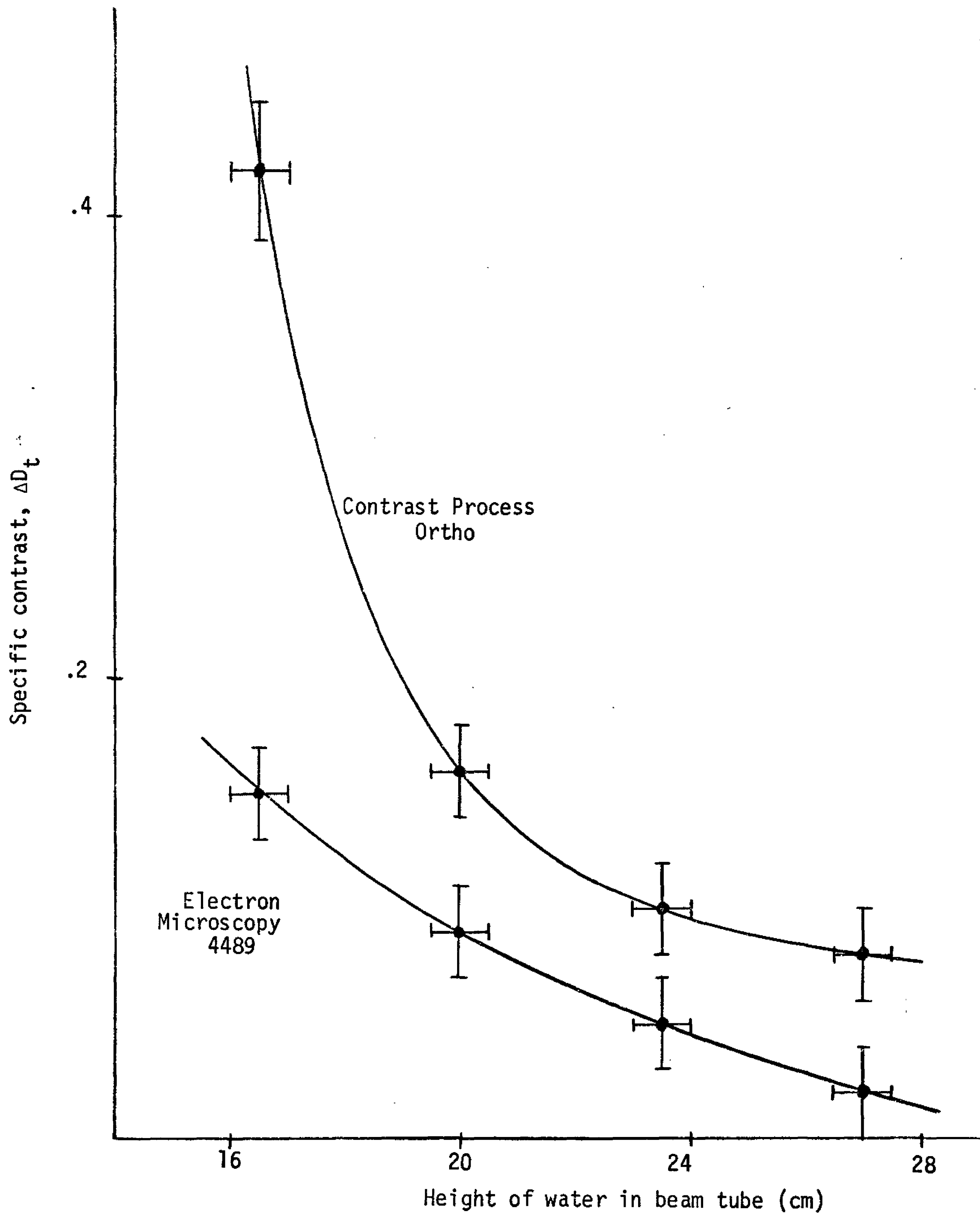

Fig. 12: Specific contrast as a function of water level, for 40 minute exposures, on Contrast Process Ortho and Electron Microscopy No. 4489 films.

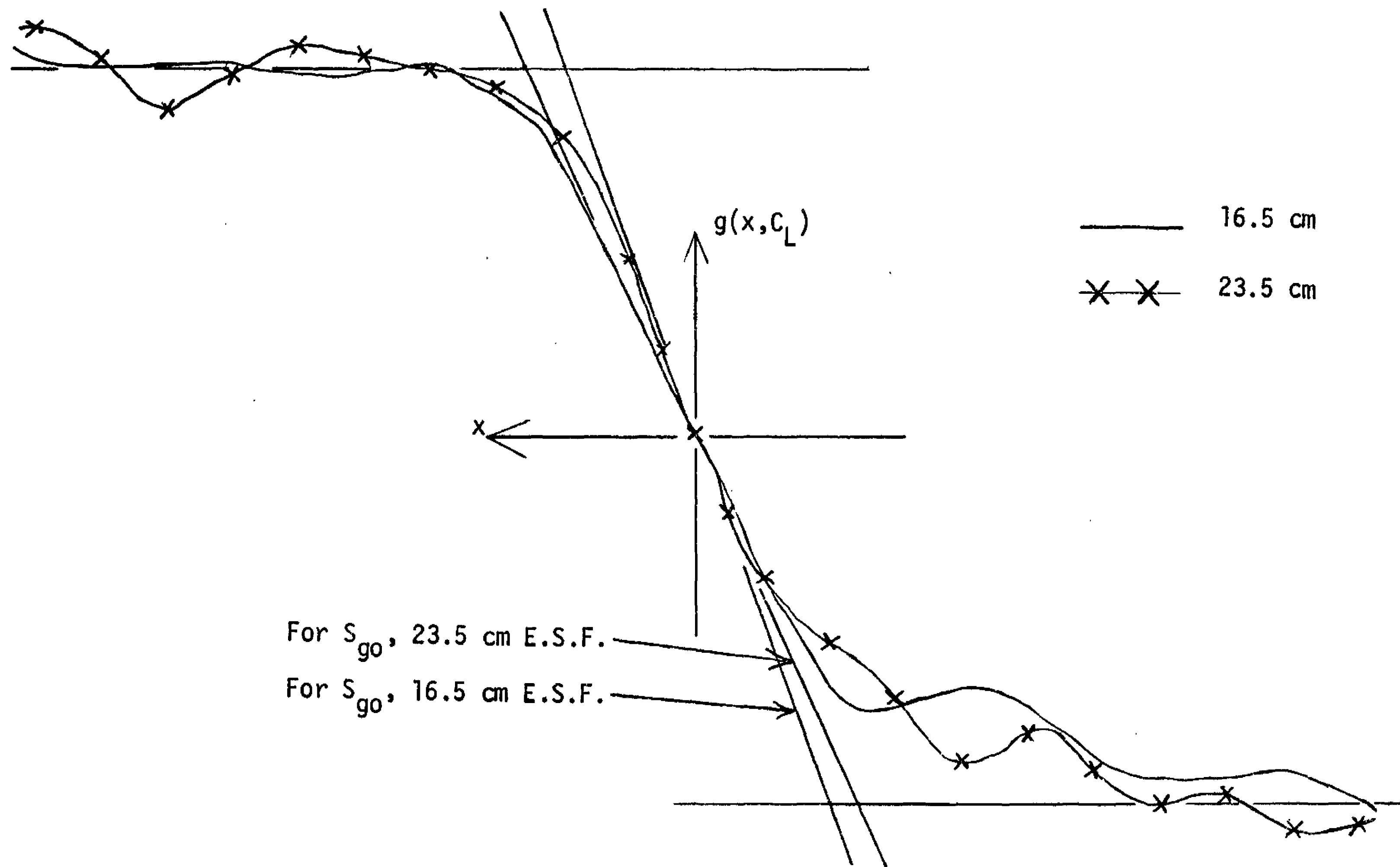

Fig. 13: Recorded edge-spread functions, type R film, 16.5 cm and 23.5 cm water levels (latter is normalized to contrast of former). The x-scale is 11.38 μ/cm.

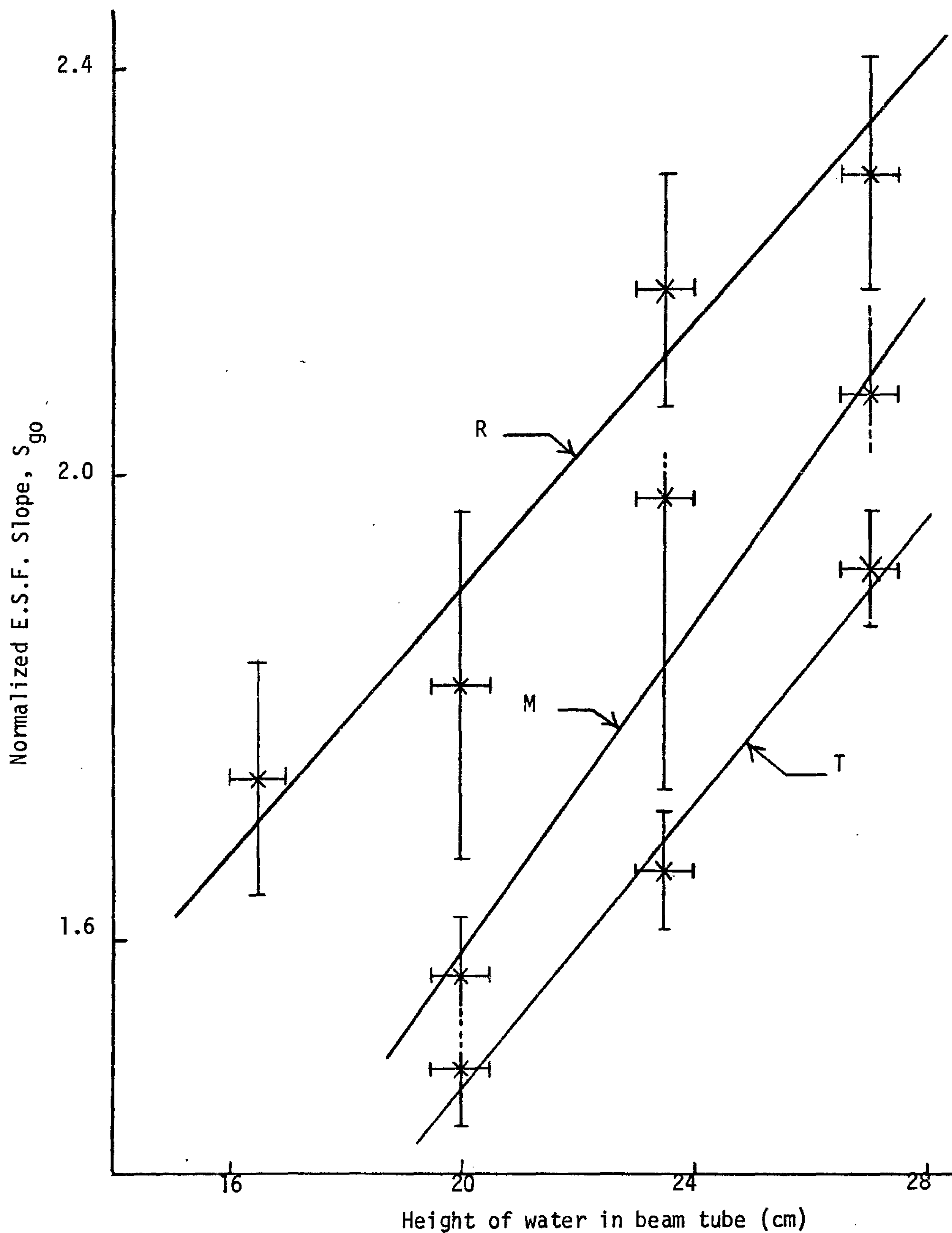

Fig. 14: Normalized slope of edge-spread function at mid-point as a function of water level, for film types R, M, and T; 40 min. exposure.

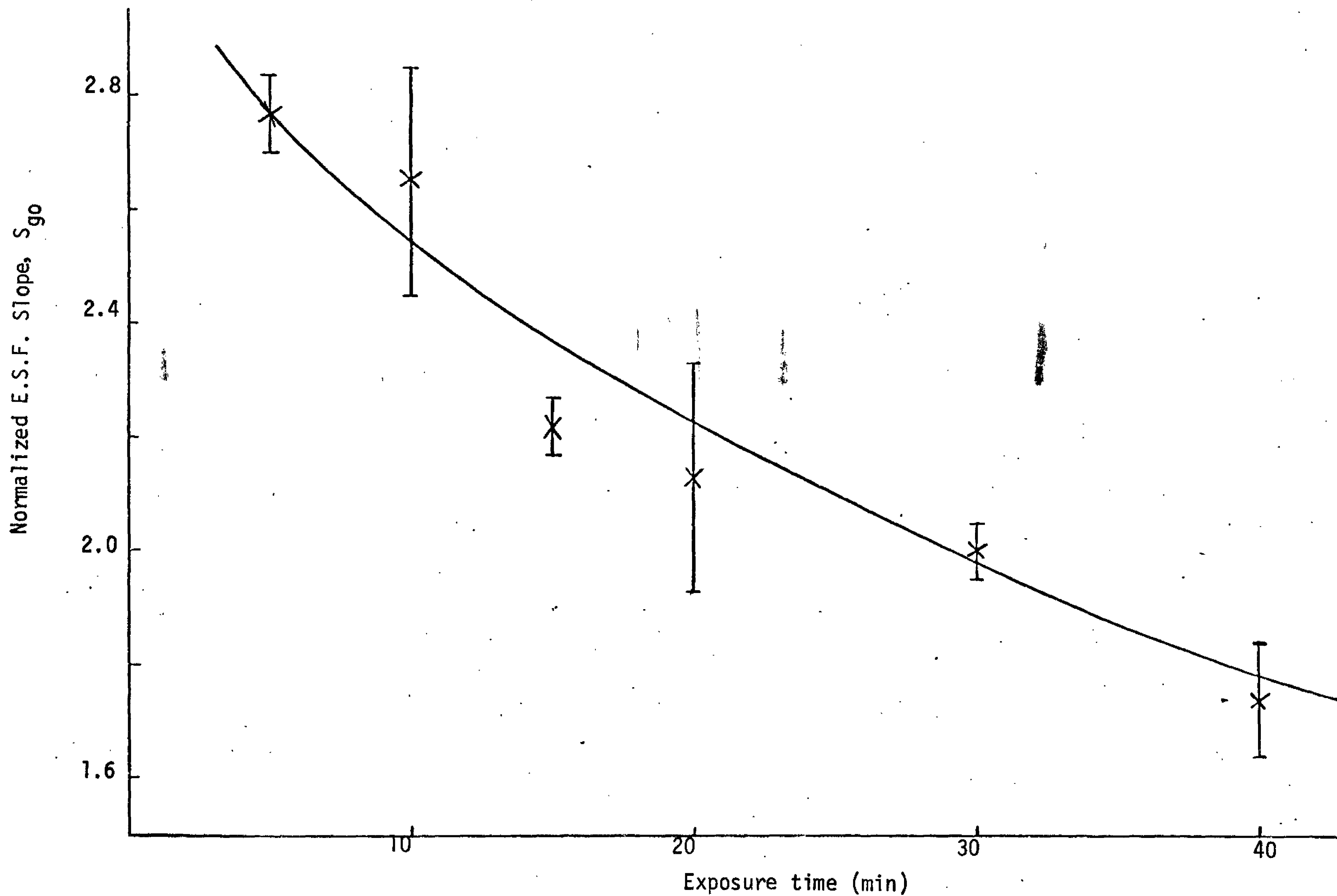

Fig. 15: Normalized mid-point slope of edge-spread function, as a function of exposure, for type R film, 16.5 cm. water level.

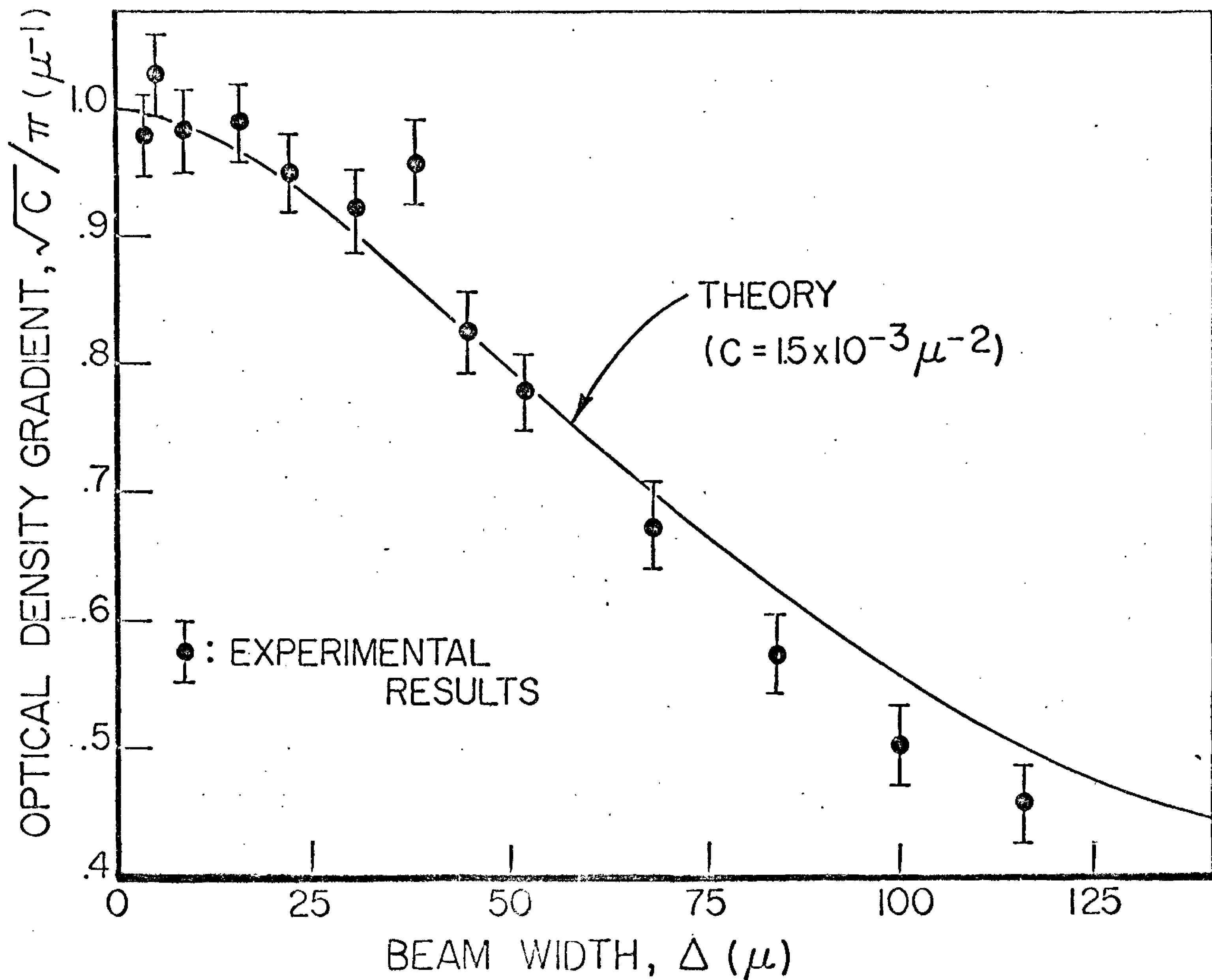

Fig. 16: Optical density gradient of a knife-edge image as a function of microdensitometer beam-width. Exposure 40 minutes, Contrast Process Ortho Film (Ref. 13).